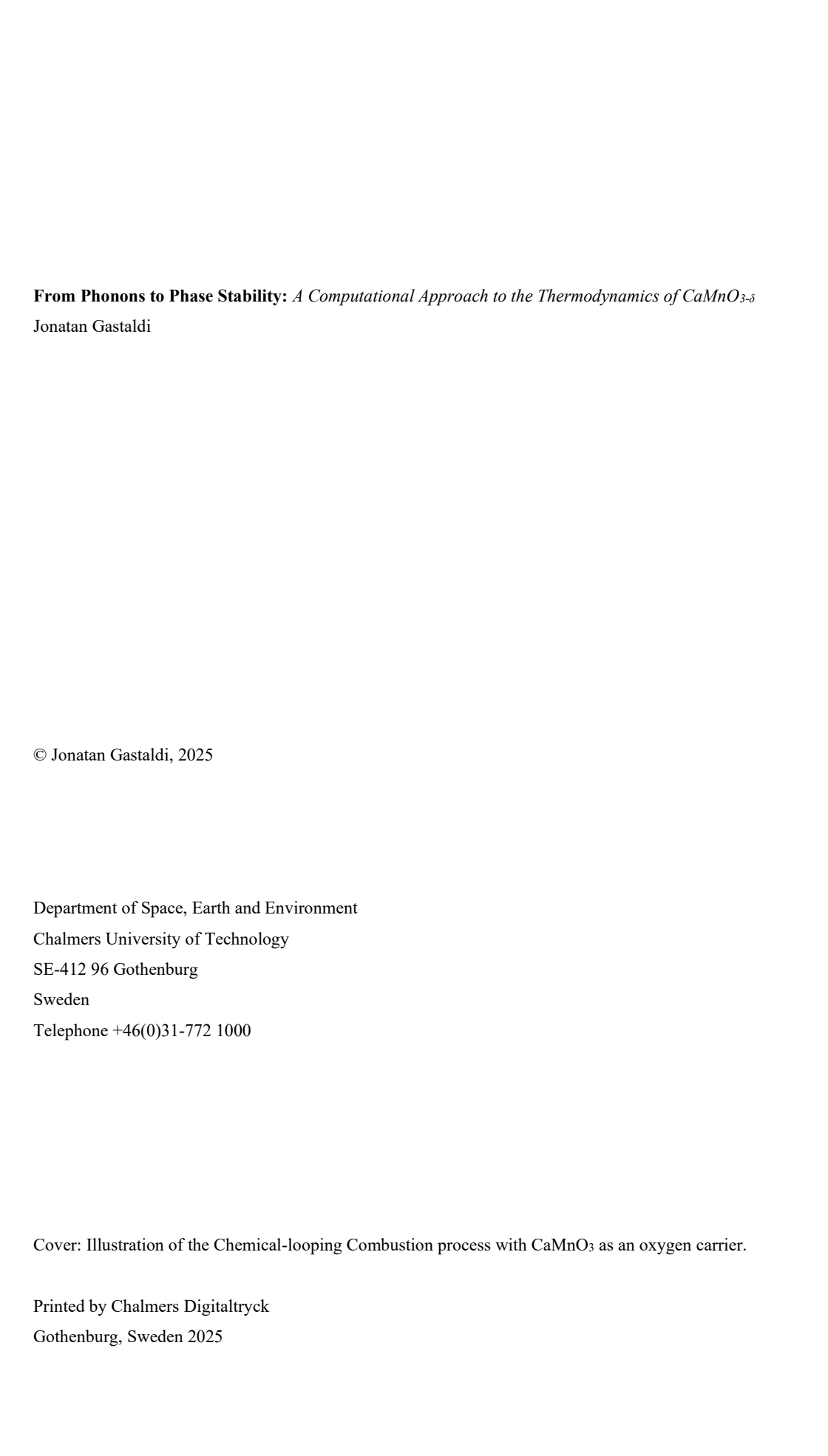
THESIS FOR THE DEGREE OF LICENTIATE OF ENGINEERING

From Phonons to Phase Stability: A Computational Approach to the Thermodynamics of CaMnO_{3- δ}

Jonatan Gastaldi

Department of Space, Earth and Environment CHALMERS UNIVERSITY OF TECHNOLOGY Gothenburg, Sweden 2025



From Phonons to Phase Stability:

A Computational Approach to the Thermodynamics of CaMnO_{3-δ}

Jonatan Gastaldi

Department of Space, Earth and Environment

Chalmers University of Technology

Abstract

The transition toward carbon-neutral energy systems requires efficient fuel conversion and

carbon capture technologies. Chemical-looping combustion (CLC) enables inherent CO₂

separation by using solid oxygen carriers that cyclically transfer oxygen between air and fuel

reactors. The performance of these materials depends on their thermodynamic and electronic

properties, which can be predicted through first-principles calculations.

This thesis presents a density functional theory (DFT)-based framework for investigating the

perovskite oxide CaMnO_{3- δ} (0 $\leq \delta \leq$ 0.5), a promising oxygen carrier for CLC applications.

Using total energy and phonon calculations, thermodynamic quantities such as heat capacities,

formation enthalpies, and Gibbs free energies were estimated and related to oxygen vacancy

formation. The results reveal how increasing oxygen deficiency affects phase stability and

electronic structure, including a transition from semiconducting to metallic behaviour and a

reduction of Mn oxidation states.

The computed formation enthalpies were combined with experimental thermodynamic data to

construct a phase diagram of the Ca-Mn-O system, providing insight into redox stability under

CLC conditions. The developed computational framework links atomic-scale modelling to

macroscopic material behaviour and offers a foundation for the predictive design of doped or

related perovskite oxygen carriers.

Keywords: Density Functional Theory (DFT), CaMnO_{3-δ}, Oxygen vacancies, Chemical-

looping combustion (CLC), Thermodynamic properties, Electronic structure, Perovskite

oxides

Ι

List of publications

The thesis is based on the following appended papers, which are referred to in the text by their assigned Roman numerals:

I. Brorsson, J., Staničić, I., Gastaldi, J., Mattison, T., & Hellman, A., Thermodynamic properties for metal oxides from first-principles. *Computational Materials Science*, 233, 112690. 2024

DOI: 10.1016/j.commatsci.2023.112690

- II. Gastaldi, J., Brorsson, J., Staničić, I., Hellman, A., & Mattisson, T., First-Principles Estimation of Thermodynamic Properties and Phase Stability of CaMnO_{3-δ} for Chemical-Looping Combustion. *Energy & Fuels*, 39(19), 9113-9120. 2025 DOI: 10.1021/acs.energyfuels.5c00267
- III. Gastaldi, J., Brorsson, J., Hellman, A., & Mattisson, T. Electronic Structure and Defect-Induced Properties of Oxygen-Deficient CaMnO_{3-δ}: Insights from First-Principles Calculations. Submitted.

Jonatan Gastaldi performed the computational work for all three papers. In Paper I, he estimated thermodynamic properties of stoichiometric CaMnO₃ using DFT and contributed to the discussions and manuscript editing. He is the principal author of Paper II, in which he carried out all DFT calculations and analyses of thermodynamic properties, including heat capacity, formation enthalpy, and entropy. In Paper III, he is also the principal author and conducted all DFT-based calculations and analyses of Gibbs free energy, electronic band structures, and related thermodynamic quantities.

Acknowledgements

The research was carried out at the Division of Energy technology at Chalmers University of Technology, Göteborg, Sweden, and was funded by the Swedish Research Council through grant agreement no. 2020-03487. The computations were enabled by resources provided by the National Academic Infrastructure for Supercomputing in Sweden (NAISS) at NSC and PDC through projects 2023/3-29, 2023/5-147, 2023/5-521, 2024/5-260.

I would like to express my sincere gratitude to my supervisors, Tobias Mattisson and Anders Hellman, for their invaluable guidance, support, and encouragement throughout this work. I also want to give a special thank you and show extra sincere gratitude to my supervisor Joakim Brorsson, who almost single-handedly helped me get started in this career and without him, this work would not have been possible. All your expertise, insightful discussions, and patience have shaped both this thesis and me as a researcher. I am deeply grateful for the time, knowledge, and trust you have invested in me.

To my colleagues at Energy technology specifically, and Chalmers in general, thank you for creating a stimulating and enjoyable working environment. The everyday discussions, shared challenges, and friendly atmosphere have made this journey not only productive but also genuinely rewarding. It has been a joy to work alongside all of you.

Finally, my heartfelt thanks go to my partner, Evgeniya, for your understanding, and patience, especially when accepting how tired I can get after work. Thank you for believing in me, and for making sure that life outside research stayed meaningful, and full of warmth.

To all of you - thank you.

Table of Contents

1	Intro	oduction	1
	1.1	Aim of the thesis	2
2	Bac	kground	3
	2.1	Energy transition	3
	2.2	Chemical-looping combustion	3
3	Met	hodology	9
	3.1	Density Functional Theory	9
	3.2	Structural properties	10
	3.3	Ground state determination	10
	3.4	Thermodynamic properties	11
	3.4.	1 Computational workflow and tools	12
	3.4.2	2 Heat capacity at constant volume	14
	3.4.3	Formation enthalpies and entropies	14
	3.4.4	4 Heat capacity at constant pressure	16
	3.5	Electronic properties	17
4	Sele	ected Results and Discussion	19
	4.1	Calculated structural properties	19
	4.2	Calculated thermal properties	21
	4.3	Phase diagram	24
	4.4	Band Structure	26
	4.5	Oxygen Vacancy formation	30
	4.6	Powder X-ray Diffraction	31
5	Con	iclusions	35
6	Futu	ure work	39
R	eferenc	res.	41

1 Introduction

The development of materials science has historically been closely intertwined with the technological progress of human civilization. Early societies relied on natural materials such as stone, wood, and clay. As technology advanced, metallurgy opened the possibility to extract and create alloys of metals such as bronze and iron. These advances were achieved through observation, experimentation, and accumulated practical knowledge rather than a systematic scientific framework. The resulting "ages" of European human history, such as the Bronze Age and the Iron Age, attest to the transformative role of materials discovery in societal development [1].

That is not to say that ideas about the nature of matter did not flourish early in human history. During the period known as Classical antiquity in Europe, Greek philosophers proposed various theories about the composition of the world, and speculation on the formation of materials can be traced back to this era [2]. It was during this time that the concept of the atom, as the smallest indivisible building block of nature, was first introduced. However, the technological limitations of the period prevented any direct investigation of these building blocks, confining such ideas to the realm of philosophy.

As Europe entered the period later referred to as the Dark Ages, much of this intellectual progress faded from mainstream discourse and was not revived until the Renaissance, when atomic ideas once again emerged. By the 16th century, technological innovation had begun to accelerate, and experimentation became increasingly central to understanding the material world. An interesting example comes from the rapid development of glassmaking in Europe during this period. Artisans learned how to produce vividly coloured glass, such as deep blue glass achieved through the refinement and use of cobalt-containing minerals, centuries before the element cobalt itself was formally identified. Their discoveries were empirical rather than theoretical, driven by experimentation rather than a formal understanding of atomic structure [2].

By the 18th century, however, major scientific advances reignited interest in atomic theory, setting the stage for a more systematic and experimental exploration of matter and its fundamental components [2]. The emergence of thermodynamics, solid-state physics, and later quantum mechanics, during the 18th to 20th centuries, transformed the study of materials from

trial-and-error experimentation into a science capable of prediction. By the mid-20th century, advances in synthesis and characterization established materials science as an interdisciplinary field, while quantum theory provided the foundation for computational methods that today enable us to link atomic-scale structure with macroscopic properties [3].

In the latter decades of the 20th century, density functional theory (DFT) made first-principles calculations of electronic structure feasible, allowing researchers to study material properties at the atomic scale without experimental synthesis [2]. Advances in computational power and algorithms have since enabled the investigation of larger, more complex systems. Today, computational methods are vital in materials science, providing accurate predictions of thermodynamic, structural, and electronic properties, as well as access to configurational spaces beyond experimental reach [4-6]. High-throughput screening and machine learning further accelerate the identification of promising materials, illustrating the shift from trial-and-error discovery to an integrated approach combining computation and experiment [7, 8].

1.1 Aim of the thesis

The aim of this thesis is to investigate the thermodynamic and electronic properties of oxide materials relevant as oxygen carriers in chemical-looping technologies. By applying first-principles computational methods, the work seeks to provide insights into the fundamental material properties that determine redox behaviour, stability, and performance. Understanding these properties at the atomic and electronic level can guide the design and selection of efficient and robust materials for oxygen carriers. The following points summarise what the thesis aims to contribute with:

- To develop a methodology for determining thermodynamic and electronic properties of oxygen carriers at finite temperatures.
- To determine the formation enthalpies, heat capacities, and entropies of model oxygen carrier materials using DFT.
- To analyse the electronic structure, including band gaps and density of states, and link these properties to material performance in chemical-looping.
- To provide insights into how fundamental thermodynamic and electronic characteristics can guide the development of stable and efficient oxygen carriers for energy technologies.

2 Background

2.1 Energy transition

The urgency of the global energy transition has once again placed materials science at the centre of technological progress. Unlike earlier eras, where materials advances were primarily driven by industrial or societal needs for stronger, lighter, or more abundant materials, the present age is defined by the urgent challenge of sustainability. Meeting global energy demands while reducing greenhouse gas emissions requires not only new energy systems but also the design of materials capable of operating under increasingly demanding or complex conditions [9, 10].

The sheer number of different energy technologies under development illustrates the breadth of material requirements. Batteries demand materials with high ionic conductivity and stability [11], catalysts enable chemical conversion [12, 13], semiconductors drive advances in photovoltaic devices [14]. In each of these domains, performance is intimately tied to the atomic-scale structure and composition of the materials employed. Thus, the ability to design and tune materials for targeted functions has become a cornerstone of modern energy research.

At the same time, the exploration of new material solutions has been accelerated by advances in computational modelling [15], high-throughput screening [16], and machine learning [17]. These approaches extend beyond incremental improvements, enabling the discovery of fundamentally new classes of materials that would be difficult to identify experimentally. The integration of computation and experiment is therefore essential not only for understanding material behaviour but also for responding effectively to the demands of the energy transition [9].

2.2 Chemical-looping combustion

Among the many approaches under investigation for sustainable energy conversion, chemical-looping combustion (CLC) represents a promising technology for power and heat generation with inherent carbon dioxide (CO₂) capture [18]. In contrast to conventional combustion, where fuel is oxidized directly with air, CLC employs a solid oxygen carrier to transfer oxygen from the air to the fuel.

This process is divided into two reactors, which are connected as shown in Figure 1:

- In the fuel reactor (FR), the oxygen carrier, MeO, oxidizes the fuel, producing a stream of CO₂ and H₂O and the reduced oxygen carrier, MeO_{1-y} returns to the AR. Since nitrogen is absent, CO₂ can be captured directly after condensing water.
- In the air reactor (AR), the reduced oxygen carrier, MeO_{1-y}, is regenerated by reacting with air, retaking its oxidized state, MeO.

This combustion route enables high efficiency while avoiding the need for energy-intensive gas separation processes post-combustion. CLC has therefore been widely studied as a pathway for low-carbon energy production, particularly in applications where large-scale CO₂ emissions are difficult to mitigate through electrification alone [19-21].

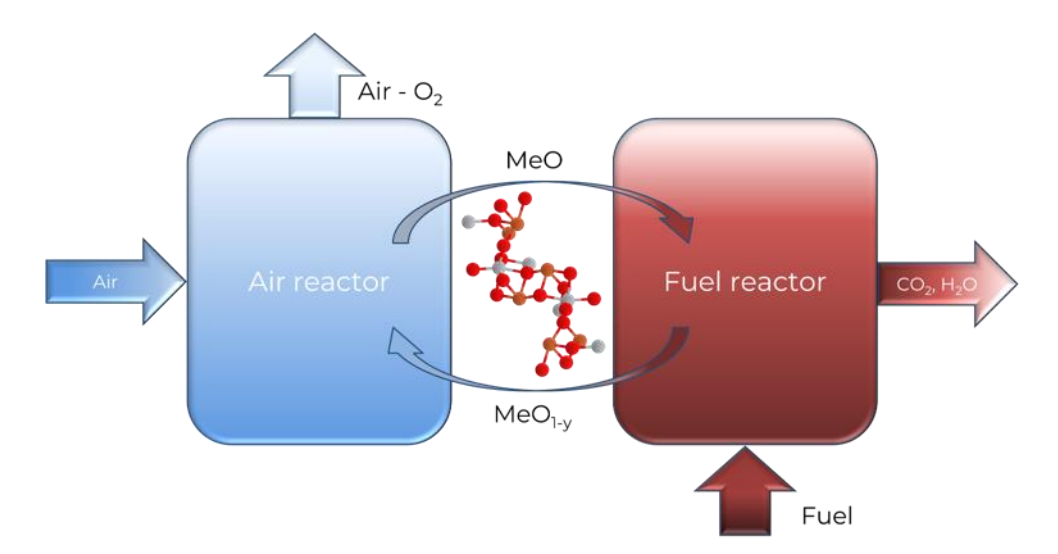


Figure 1 Schematic illustration of the CLC process. The oxygen carrier circulates between the air reactor and the fuel reactor, transferring oxygen to the fuel without direct contact between air and fuel, thereby enabling inherent CO_2 separation. In this illustration, the oxygen carrier is visualized as ilmenite (FeTiO₃).

The technical feasibility of CLC depends critically on the performance of the oxygen carrier material. The carrier must withstand repeated redox cycles, transfer sufficient amounts of oxygen per cycle, and remain stable under high-temperature operating conditions [18]. These requirements place challenging demands on materials design and make the development of suitable oxygen carriers one of the central scientific challenges for advancing chemical-looping technology.

The oxygen carrier is one of the fundamental aspects of CLC. Its performance directly determines the efficiency, durability, and scalability of the process. A good oxygen carrier must have several distinct properties [22]:

- High oxygen transfer capacity, to maximize fuel conversion efficiency.
- High thermochemical stability, to withstand repeated redox cycling at elevated temperatures.
- High mechanical resistance, to avoid attrition and loss of active material in fluidized systems.
- Tunability of redox thermodynamics, to enable operation with different fuels and under varying process conditions.

Meeting these criteria simultaneously remains a challenge. The development of oxygen carriers (OCs) for CLC has evolved significantly over the past two decades. Early studies focused on simple metal oxides, such as those of Fe [23], Ni [24], Cu [25], and Mn [26], or a combination of these transition metals [22, 27-30], due to their ability to undergo reversible redox reactions with gaseous oxygen. However, these materials often suffered from issues such as sintering, low mechanical stability, and loss of reactivity during repeated cycling [22]. The search for more robust materials led to an increased interest in complex oxides, particularly ilmenite and perovskite-type structures [31-34], the latter being the main focus of the current work [35].

Perovskite oxides (ABO₃) have attracted particular attention due to their structural flexibility and tuneable redox properties. The perovskite structure can accommodate a broad range of A-and B-site cations, as well as variable oxygen stoichiometry, which makes it highly adaptable to different operating environments. This versatility enables perovskites to exhibit oxygen transport characteristics not easily accessible in simpler oxide systems.

Within this family of materials, calcium manganite (CaMnO₃), see **Figure 2**, has emerged as a promising candidate as an oxygen carrier. It combines several favourable attributes: abundance of constituent elements, relatively low cost, and the ability to undergo reversible reduction through the formation of oxygen vacancies [22]. The oxygen non-stoichiometry, expressed as CaMnO_{3-δ}, directly governs its redox capacity and thermodynamic behaviour. Understanding this defect chemistry is therefore central to assessing its suitability as an oxygen carrier.

However, the performance of CaMnO₃ is influenced by a complex interplay of structural, electronic, and thermodynamic factors. Oxygen vacancy formation affects not only oxygen transport capacity but also phase stability and electronic structure. Moreover, the redox thermodynamics of CaMnO₃ are sensitive to temperature, pressure, and the local coordination environment of manganese, which can undergo multiple oxidation states. These intricacies present difficult challenges for experimental exploration, particularly given the need to map wide configurational spaces.

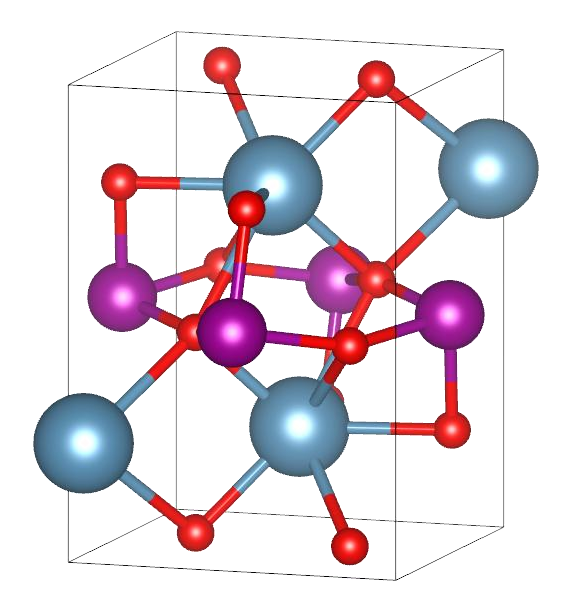


Figure 2 Unit cell of Orthorhombic CaMnO₃. The blue atoms represent Calcium (Ca), the purple atoms represent Manganese (Mn), and the red atoms represents oxygen (O).

The ability of CaMnO₃ to accommodate oxygen vacancies without collapsing the perovskite framework makes it especially promising for redox-based energy applications. Experimental studies have characterized its redox behaviour under varying oxygen partial pressures and temperatures. Rørmark et al. [36] and Bakken et al. [37], among others, have reported thermodynamic data such as enthalpy of formation and heat capacity, providing important benchmarks for both fundamental understanding and modelling efforts. Experimental investigations of CaMnO₃ in CLC conditions have shown that it maintains reasonable structural integrity over multiple redox cycles, though phase transformations to other oxides such as Ca₂MnO₄ or CaMn₂O₄ can occur under reducing conditions [22].

Computational methods have played an increasingly central role in studying CaMnO₃ and related materials, offering atomistic insights into their redox and electronic properties. DFT calculations have been used to estimate formation enthalpies, defect formation energies, and oxygen vacancy migration barriers, as well as to explore the relationship between magnetic ordering and electronic structure [38-42]. These studies have clarified that the creation of oxygen vacancies leads to mixed valence states of manganese, typically involving a reduction from Mn⁴⁺ to Mn³⁺, which in turn affects both the electronic band structure and magnetic interactions. However, despite these advances, significant challenges remain. Calculated formation enthalpies often deviate from experimental values, with discrepancies depending on

the choice of exchange-correlation functional. For instance, while GGA+U calculations can capture some aspects of the electronic structure, they tend to overestimate formation enthalpies, whereas meta-GGA functionals such as SCAN and r²SCAN improve agreement but still show residual deviations [38]. These inconsistencies complicate direct comparison with experimental thermodynamic data and underscore the need for improved computational approaches.

Earlier computational studies on CaMnO₃ often focused either on thermodynamic or electronic properties in isolation depending on the focus of each study, the interplay between these two aspects is essential for understanding how oxygen vacancies influence redox activity and material stability, which is central for oxygen carriers in CLC. Furthermore, most DFT-based studies have focused on stoichiometric CaMnO₃ or a limited set of vacancy concentrations, leaving a gap in the systematic treatment of the entire CaMnO_{3-δ} system. Experimental efforts to construct phase diagrams have also been constrained by the challenges of measuring oxygen nonstoichiometric and phase-equilibria under CLC-relevant conditions.

This challenge highlights the vital role of modern materials science. Advanced computational methods such as DFT allow the thermodynamic and electronic properties of candidate oxygen carriers to be investigated at the atomic scale. When combined with phonon modelling, these approaches can provide estimates of key thermodynamic quantities such as heat capacity, entropy, and enthalpy as functions of temperature. The next step would then be experimental synthesis and characterization; these approaches enable a rational search for materials that balance oxygen transfer capability with thermal and mechanical stability. Ultimately, the development of robust oxygen carriers represents not only a materials discovery problem but also a bottleneck that must be overcome for CLC to become a viable technology in the energy transition.

In summary, previous work has established CaMnO₃ as a promising oxygen carrier and provided valuable insights into its redox behaviour and structural evolution. However, a consistent, quantitative framework that unifies thermodynamic, structural, and electronic perspectives is still lacking. The present thesis builds upon this foundation by combining first-principles thermodynamic modelling with electronic structure analysis to explore the behaviour of CaMnO_{3-δ} across a range of oxygen vacancy concentrations. This integrated approach aims to bridge the gap between computational prediction and experimental observation, contributing to a more complete understanding of the material's potential in chemical-looping applications.

3 Methodology

3.1 Density Functional Theory

DFT is a quantum mechanical method used to calculate the electronic structure and total energy of materials from first-principles. It is based on the Hohenberg-Kohn theorems, which establish that the ground-state properties of a many-electron system are uniquely determined by its electron density, and that the total energy can be expressed as a functional of this density [43]. In practice, the Kohn–Sham formalism reformulates the complex many-body problem into a set of single-particle equations that are solved self-consistently [44]. The accuracy of DFT depends largely on the choice of exchange-correlation functional, which approximates all effects beyond the classical electron-electron interaction, including exchange, correlation, and self-interaction corrections. DFT provides an effective balance between accuracy and computational cost, making it a widely used tool for predicting structural, thermodynamic, and electronic properties of solids which has been proven repeatedly during the past few decades [45].

DFT, as implemented in VASP [46] (version 5.4.4), was used for all first-principles calculations required to evaluate the methodology, which includes structure relaxations and force determinations. The input files were, more precisely, generated with PYMATGEN [47]. This ensured that the settings were the same as in the Materials Project [48], which entailed using the generalized gradient approximation (GGA) functionals presented by Perdew, Burke and Ernzerhof [49] and an energy cutoff of 520 eV, as well as setting the U-value for Mn to 3.9 eV [47]. Initially, the energy difference for the electronic and ionic convergence was set to 10^{-3} eV and 10^{-2} eV per atom, respectively. After this, a second relaxation was performed using the same functionals, to achieve more accurate results, where the same thresholds were set to 10^{-6} eV and 10^{-5} eV, respectively. In addition, structure relaxations using SCAN and r^2 SCAN functionals were done for stoichiometric CaMnO₃. Specifically, the purpose was to determine the difference in free energy when using more detailed functionals than GGA+U.

To generate a reciprocal grid of k-points, the Monkhorst-Pack method was used for the stoichiometric CaMnO₃. For each oxygen vacancy concentration, the Gamma-centred method was used. A reciprocal grid of 1100 k-points per atom was used, which is higher than the default setting in the Materials Project (1000). The tetrahedron method with Blöchl correction was used to sample the grid for all compositions.

This study concerns the following compositions with different fractions of vacancies: CaMnO₃, CaMnO_{2.9375}, CaMnO_{2.875}, CaMnO_{2.8125}, CaMnO_{2.75}, CaMnO_{2.6875}, CaMnO_{2.625}, CaMnO_{2.5625}, CaMnO_{2.5625}, CaMnO_{2.5625}. To represent different oxygen vacancy concentrations, unit cells with up to 80 atoms had to be used, specifically Ca₁₆Mn₁₆O₄₈, Ca₁₆Mn₁₆O₄₇, Ca₁₆Mn₁₆O₄₆, Ca₁₆Mn₁₆O₄₅, Ca₁₆Mn₁₆O₄₄, Ca₁₆Mn₁₆O₄₃, Ca₁₆Mn₁₆O₄₂, Ca₁₆Mn₁₆O₄₁, and Ca₁₆Mn₁₆O₄₀.

3.2 Structural properties

The structural properties of a material determine its stability, mechanical behaviour, and influence many of its electronic and thermodynamic properties. In DFT calculations, the equilibrium structure is obtained by minimizing the total energy of the system with respect to both atomic positions and lattice parameters. This corresponds to finding the local minimum on the potential energy surface, in which all atomic forces vanish, and the system experiences no net stress. Structural optimization, therefore, involves iteratively solving the Kohn–Sham equations while adjusting the atomic geometry to minimize this total energy.

Crystal symmetry and bonding topology also play a role in determining physical properties. For perovskite oxides, for example, distortions of the BO₆ octahedra (tilts, rotations, or Jahn–Teller distortions) strongly affect both the electronic bandwidth and the magnetic exchange interactions. Even subtle structural changes, such as those induced by oxygen vacancies or cation substitution, can modify the band gap and oxidation energetics.

In the context of this work, accurate structural optimization is essential to ensure reliable evaluation of total energies, electronic structures, and thermodynamic quantities because small inaccuracies in structural relaxation can propagate into significant errors in estimated properties.

3.3 Ground state determination

Here, the term 'ground state' refers to the lowest-energy configuration across all considered oxygen vacancy arrangements at a given composition, as obtained from a cluster expansion (CE) and mixed integer programming (MIP) procedure.

Cluster expansion (CE) is an efficient method for estimating the ground state energy by exploiting the repeating symmetry patterns in a crystal structure and incorporating machine learning techniques. By using machine learning, the cluster expansion learns to recognize how the energy of a structure changes depending on how the repeating symmetry patterns lie in a crystal and makes an estimation as to which is the lowest energy structure even though it does

not need to have done calculations on all potential configurations. The ICET toolkit [50] was used to find the ground state structures with oxygen vacancies via the creation of alloy CEs. This method is often used to represent disordered systems as combinations of clusters with different symmetries. Based on the order, or, in other words, the number of atoms per cluster, these can be classified as pairs, triplets, quadruplets, and so on. Since the number of possible clusters is theoretically infinite, practical implementations of the method include only clusters up to a certain order, while clusters with larger radii than a defined cutoff are disregarded. In practice, however, the selection is often limited by the available computational resources as well as the size of the training data set.

For the training dataset, 200 configurations were created by randomly replacing oxygen atoms in up to 40 atom CaMnO_{3-δ} supercells with vacancies. After relaxing the structures as detailed below, a CE, with cutoffs of 3.5 Å for pairs and 1.5 Å for triplets, was fitted using automatic relevance detection regression (ARDR). The ground states were then determined using a procedure based on MIP, as shown by Larsen et al. [51] and Brorsson et al. [52], which is implemented in ICET [50].

3.4 Thermodynamic properties

The thermodynamic properties of a material describe its energetic stability and the response of its internal energy to changes in temperature, pressure, and composition. In the context of solid-state materials, these properties can be derived from first-principles calculations of total energies, phonon spectra, and defect energetics. Such quantities form the basis for evaluating the relative stability of compounds, predicting phase equilibria, and estimating the energy requirements for redox reactions.

For the systems considered in this thesis, thermodynamic quantities were obtained by extrapolating properties from the total energies of the studied compounds to their corresponding elements or competing phases according to the general chemical balance shown in Equation (1),

$$CaMnO_{3-\delta} + (2-3\delta)MnO = CaO + (1-\delta)Mn_3O_4.$$
 (1)

Where δ is the measurement for oxygen vacancy concentration of CaMnO₃. This chemical balance does not describe a reaction but instead it is a balance of the constituent elements and is built up by the compound that is studied, CaMnO_{3- δ}, and three well-known monometallic oxides. These monometallic oxides have been thoroughly studied, and their properties are well known and agreed upon by the scientific community.

This relation provides a consistent foundation for deriving quantities such as the formation enthalpy, entropy, and heat capacity presented in the following sections.

3.4.1 Computational workflow and tools

To calculate the thermodynamic properties this thesis used a method presented in **Paper I** and expanded in **Paper II**, with the addition of accounting for oxygen vacancies in the studied material. The method, which is presented in **Figure 3**, was originally proposed by Benisek and Dachs, which they used to estimate properties of materials which are considered interesting in petrology, and is based on DFT calculations [53]. Generally, the starting point is the crystal structure of the material of interest. After using DFT to find the lowest energy state, it is possible to estimate the phononic contribution of the heat capacity based on the harmonic approximation. When combined with the 0 K energies from the DFT calculations, an estimation of the reaction enthalpy at 298.15 K can be obtained. By using the results together with tabulated thermodynamic properties of well-known simple metal oxides, it is possible to determine the temperature dependent specific heat capacity, together with the entropy and the formation enthalpy at 298.15 K. Benisek and Dachs was only interested in exploring the properties at rooms temperature, the method development presented in this thesis include the possibility to explore the materials at higher temperatures.

For a crystal in which multiple species, i.e. oxygen vacancies, occupy the same lattice sites, cluster expansions (CE) were trained in order to find the ground state for each oxygen vacancy concentration, as was explained in section 3.3 [50]. The method is the same as that employed for systems with only one species per lattice site. In the former case, it is also possible to use the CE to perform Monte-Carlo simulations and thereby estimate the contribution of chemical ordering to the heat capacity [50].

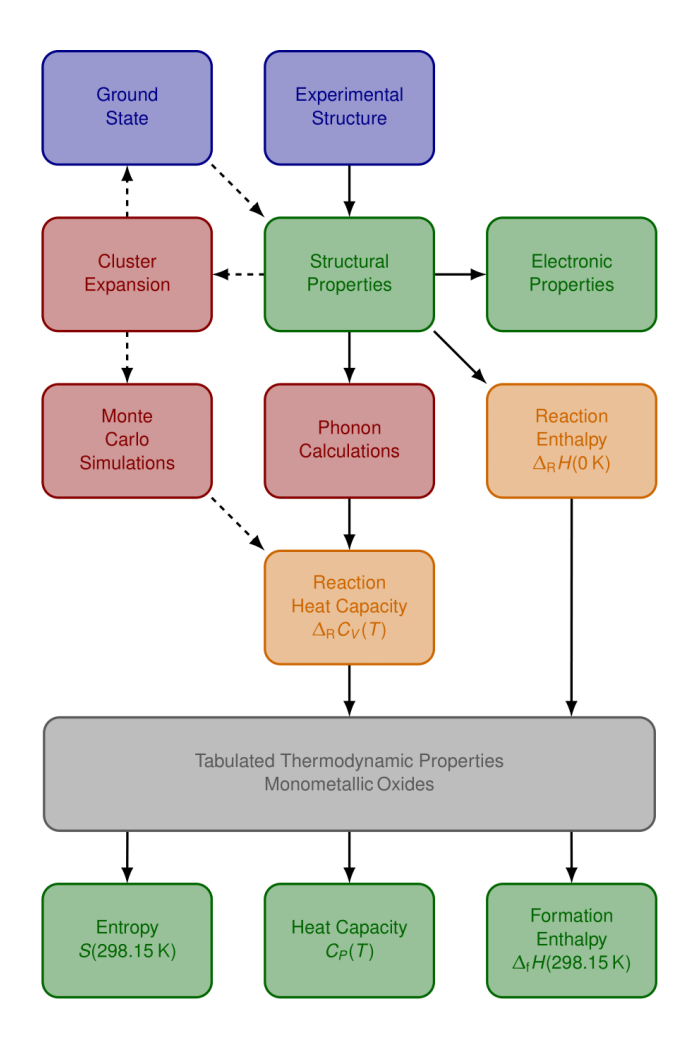


Figure 3 Schematic illustration of the procedure for estimating the entropy, formation enthalpy, and heat capacity by combining first-principles calculations and tabulated experimental data for monometallic oxides. Specifically, the main (optional) steps are indicated by the solid (dashed) arrows, while the blue, red, orange, grey, and green blocks represent external data, computational methods, intermediate results, data from other sources, and results, respectively. The optional steps are only required when the ground state of the material is not known, which is the case for structures with vacancies.

The phononic contribution to the heat capacity was estimated using the PHONOPY [54] package based on force constants (FCs) that were determined using HIPHIVE [55]. Fifteen "rattled" supercells, with up to 200 atoms, were generated from the ground state structure for each oxygen vacancy concentration by randomly displacing all atoms by distances drawn from a Gaussian distribution with a 0.02 Å standard deviation. Note that the primitive unit cell was repeated the same number of times for all vacancy concentrations. In the case of Ca₁₆Mn₁₆O₄₇, for instance, the supercells consisted of 158 atoms. The interatomic forces, obtained from a static calculation in VASP, were used, together with the displacements, to fit the force constant potentials (FCPs). By using the force constants (FCs) extracted from the FCPs, the thermodynamic properties were calculated from 10 K up to 2500 K based on a uniform mesh with 5x10⁶ q-points per reciprocal atom.

3.4.2 Heat capacity at constant volume

The heat capacity reflects the ability of a material to store thermal energy and is a key parameter for describing its temperature-dependent thermodynamic behaviour. In crystalline solids, the dominant contribution to the heat capacity at ordinary temperatures arises from lattice vibrations, or phonons. Within the harmonic approximation, the phonon contribution to the constant-volume heat capacity, C_V, can be obtained according to Equation (2) [54]

$$C_V(T) = \left(\frac{\partial E}{\partial T}\right)_V = \sum_{q\nu} k_B \left(\frac{\hbar\omega(q\nu)}{k_B T}\right)^2 \frac{e^{\hbar\omega(q\nu)/(k_B T)}}{(e^{\hbar\omega(q\nu)/(k_B T)} - 1)^2},\tag{2}$$

where ω is the phonon frequency, \hbar is the reduced Planck constant, k_B is the Boltzmann constant, and T is the temperature. The sum is taken over each specific phonon mode, q, at a particular wave vector, ν .

The phonon spectra were computed using the finite-displacement method as implemented in Phonopy, based on forces calculated with VASP. Structural optimizations were first performed to ensure forces below a given threshold, after which atomic displacements were introduced to generate force constants and construct the dynamical matrix. The phonon density of states obtained from diagonalization of this matrix was then used to calculate the heat capacity as a function of temperature.

To account for the thermodynamic effects of oxygen-vacancy ordering, we supplement the harmonic lattice heat capacity with a configurational contribution obtained from Monte Carlo sampling using the MCHAMMER module from ICET [50]. This approach allows us to capture ordering effects that are not described in a purely harmonic framework, providing a more complete picture of the thermodynamics of CaMnO_{3-δ}.

By using the chemical balance determined in Equation (1) and calculating the heat capacity of each of the components, it is then possible to estimate the heat capacity of the reaction using Equation (3) as this will be important when estimating the enthalpy and entropy of formation.

$$\Delta_R C_V = C_{V,\text{CaMnO}_{3-\delta}} - \left(C_{V,\text{CaO}} + (1-\delta)C_{V,\text{Mn}_3O_4} - (2-3\delta)C_{V,\text{Mn}_O} \right).$$
 (3)

3.4.3 Formation enthalpies and entropies

The formation enthalpy provides a quantitative measure of the relative thermodynamic stability of a compound. It reflects the energy change associated with forming a material from its reference phases or materials and thus serves as a key descriptor for assessing phase stability

and reactivity. In the context of this work, formation enthalpies are used to evaluate the relative stability of Ca-Mn-O compounds and to compare results obtained from DFT with available theoretical and experimental data.

The formation enthalpy $(\Delta_f H)$ was calculated based on the total energies from CaMnO_{3- δ} and relevant metal oxides based on the chemical balance described in Equation (1)

This balance can then be used to estimate the enthalpy of reaction at $0 \text{ K} (\Delta_R H^{0K})$ by assuming that it can be equal to the difference of the energy of the ground states of each crystal structure according to Equation (4)

$$\begin{split} \Delta_R H^{0K} &= \Delta_R U^{0K} + P \Delta_R V^{0K} \approx \Delta_R U^{0K} \\ &= U^{0K}_{\mathsf{CaMnO}_{3-\delta}} - \left(U^{0K}_{\mathsf{CaO}} + (1-\delta) U^{0K}_{\mathsf{Mn}_3\mathsf{O}_4} - (2-3\delta) U^{0K}_{\mathsf{MnO}} \right). \end{split} \tag{4}$$

In order to bring this into more real applications the reaction enthalpy and entropy at room temperature is determined to be

$$\Delta_R H^{298.15K} \approx \Delta_R H^{0K} + \int_0^{298.15} \Delta_R C_V dT,$$
 (5)

$$\Delta_R S^{298.15K} \approx \Delta_R S^{0K} + \int_0^{298.15} \frac{\Delta_R C_V}{T} dT.$$
 (6)

Where $\Delta_R S^{0K}$ is assumed to be 0 at 0 K. Since the monometallic oxides are well known and have tabulated formation enthalpies it is possible to estimate the enthalpy of formation accurately using the reaction enthalpy together with the formation enthalpies and entropies of the monometallic oxides according to Equations (7) and (8)

$$\Delta_f H^{298.15K} = \Delta_R H^{298.15K} + \Delta_f H_{Ca0}^{298.5K} + (1 - \delta) \Delta_f H_{Mn_3O_4}^{298.5K}$$

$$- (2 - 3\delta) \Delta_f H_{Mn_0}^{298.5K},$$
(7)

$$S^{298.15K} = \Delta_R S^{298.15K} + S_{CaO}^{298.15K} + (1 - \delta) S_{Mn_3O_4}^{298.15K} - (2 - 3\delta) S_{MnO}^{298.15K}.$$
 (8)

While Benisek and Dachs only used the above procedure to estimate properties at room temperature, **Paper I** showed how this approach can be extended to include the heat capacity

at elevated temperatures. Specifically, it is assumed that the following two expressions of the enthalpy of formation are equal:

$$\Delta_f H^T = \Delta_f H^{0K} + \int_0^T C_P dT', \tag{9}$$

$$\Delta_{f}H^{T} \approx \Delta_{R}H^{0K} + \int_{0}^{T} \Delta_{R} C_{V}dT' + \Delta_{f}H_{CaO}^{T} + (1 - \delta)\Delta_{f}H_{Mn_{3}O_{4}}^{T}$$

$$- (2 - 3\delta)\Delta_{f}H_{MnO}^{T}.$$
(10)

3.4.4 Heat capacity at constant pressure

As a final step in the methodology of the thermodynamic properties, the heat capacity at constant pressure, C_p , for CaMnO_{3- δ} is determined using Equation (11)

$$\int_{0}^{T} C_{p} dT' \approx \Delta_{R} H^{0K} + \int_{0}^{T} \Delta_{R} C_{V} dT' + \Delta_{f} H_{CaO}^{T} + (1 - \delta) \Delta_{f} H_{Mn_{3}O_{4}}^{T}$$

$$- (2 - 3\delta) \Delta_{f} H_{MnO}^{T} - \Delta_{f} H^{0K}.$$
(11)

Crucially, tabulated reference data for the monometallic oxides is used to increase the accuracy. The reference data for CaO was taken from the NIST-JANAF thermochemical tables, and the data for Mn₃O₄ and MnO from other publications [56, 57]. Since the formation enthalpies are given by

$$\Delta_f H_X^T = \Delta_f H_X^0 + \int_0^T C_{p,X} \, dT', \tag{12}$$

where X = CaO, Mn_3O_4 , and MnO, the expression for the heat capacity, of the compound of interest, in Equation (11) can be reduced to

$$C_P(T) \approx \Delta_R C_V(T) + C_{P,CaO}(T) + (1 - \delta)C_{P,Mn_3O_4}(T) - (2 - 3\delta)C_{P,MnO}(T).$$
 (13)

To use the results together with other components and phases, such as those incorporated in the multi-component, multi-phase equilibrium software FactSage 8.2 [58], it is necessary to express the specific heat capacity, at constant pressure, as a function of temperature using a series of power functions with a maximum of eight terms,

$$C_P(T) = \sum_{i=1}^8 k_i T^{P_i}.$$
 (14)

In this study, five terms were used to estimate the heat capacity of CaMnO_{3-δ},

$$C_P(T) = k_0 + k_1 T^{-0.5} + k_2 T^{-3} + k_3 T^{-2} + k_4 T^{-1}.$$
 (15)

3.5 Electronic properties

The electronic properties of crystalline materials can be understood in terms of their band structure, which describes the allowed energy levels of electrons as a function of momentum. A central feature of the band structure is the energy gap (Eg) between the valence band (highest occupied electronic states), VBM, and the conduction band (lowest unoccupied electronic states), CBM [59]. The size of this gap determines whether a material behaves as a metal, semiconductor, or insulator and is shown in **Figure 4**.

Schematic Band Structures

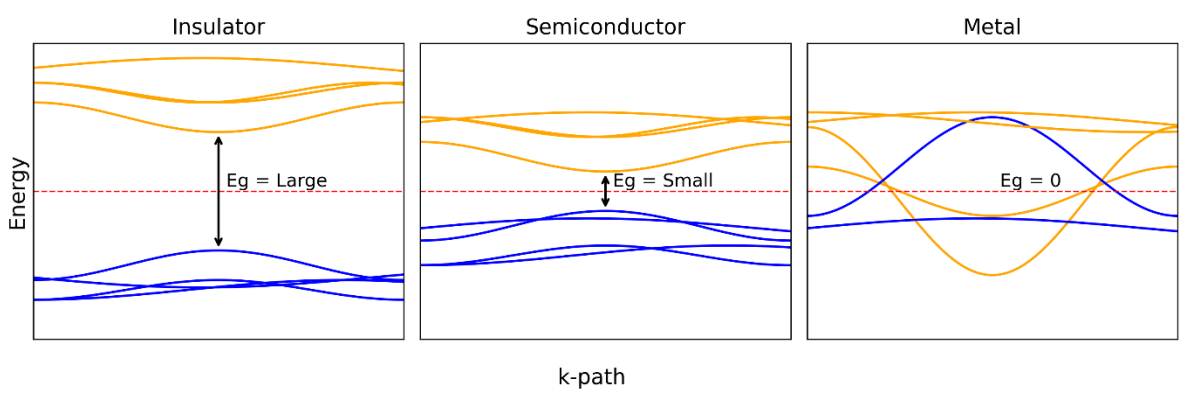


Figure 4 The figure shows how band structures may appear for different material types. It is a purely conceptual illustration and does not correspond to any specific material. VBM is represented by blue lines, CBM as orange lines.

Metals are characterized by a vanishing band gap (Eg=0). Their valence and conduction bands overlap, or the Fermi level intersects partially filled bands. This allows electrons to move freely under an applied electric field, giving rise to high electrical conductivity.

Semiconductors possess a finite but moderate band gap. At low temperatures, the valence band is filled, and the conduction band is empty, resulting in low conductivity. However, electrons can be thermally excited across the gap, and conductivity can be further tuned by introducing impurities (doping).

Insulators have a large band gap, which makes thermal excitation of electrons into the conduction band negligible under normal conditions. As a result, insulators exhibit very low electrical conductivity.

Understanding these classes is important not only from a fundamental standpoint but also for technological applications. In materials discovery, band structure analysis provides a direct way of predicting a material's functionality. For example, in energy technologies such as chemical-looping, the electronic structure could potentially influence oxygen vacancy formation, redox activity, and overall stability. Thus, careful classification of materials based on their band structure is a first step toward linking electronic properties to performance in specific applications.

After relaxing the structures using GGA+U, as laid out in section 3.2, a non-self-consistent calculation was performed using the Modified Becke-Johnson (MBJ) MetaGGA potential [60]. The reason for this is that the MBJ potential has been shown to reproduce experimentally determined electronic band structures of crystals more accurately than using GGA+U [60, 61]. The MBJ calculations were performed with the same level of accuracy as the relaxations described in Section 3.1. The band structure was calculated along the high-symmetry Brillouin zone path Γ —X—S—Y— Γ —Z—U—R—T—Z, which is continuous for members of space group 62 (Pnma), such as orthorhombic CaMnO₃, and visualized using the Python toolkit Sumo [62].

4 Selected Results and Discussion

4.1 Calculated structural properties

The optimized lattice parameters of stoichiometric CaMnO₃ obtained in this work are compared with both experimental measurements and previous computational studies in **Table 1**. The calculated lattice constants (a = 5.325 Å, b = 5.398 Å, and c = 7.554 Å) are slightly larger than the experimental and theoretical values reported in earlier studies, but overall, the results fall within the expected range and are considered to be in good agreement with both experimental and theoretical references.

Table 1 Comparison of lattice parameters for stoichiometric CaMnO₃.

δ	Exp. [63]	Exp. [36]	Calc. [41]	Calc. [64]	This work
a (Å)	5.264	5.286	5.316	5.314	5.325
b (Å)	5.279	5.292	5.380	5.367	5.398
c (Å)	7.448	7.463	7.543	7.548	7.554
$V(Å^3)$	206.97	208.77	215.73	215.26	217.11

The computed unit cell volume (217.11 ų) is marginally larger than those reported in the literature, consistent with the slight overestimation of lattice parameters observed in DFT calculations using the GGA+U functional. Such deviations are typical and remain within acceptable limits for first-principles methods, it should also be noted that the cited results from calculations was done using antiferromagnetic configuration of the materials magnetism, this work is using ferromagnetic magnetism. There are no results in literature regarding ferromagnetic CaMnO₃. The choice of exchange–correlation functional, together with assumptions about magnetic ordering, can influence the predicted lattice dimensions. In this work, a ferromagnetic configuration was assumed, whereas experimental studies may involve antiferromagnetic or mixed states. The theoretical studies cited here used antiferromagnetic configuration, which could be a reason for the discrepancy. Small deviations in oxygen stoichiometry or unplanned doping in experimental samples can also affect lattice constants, while the simulations assume perfect stoichiometry. Minor methodological differences, such

as k-point sampling, energy cutoffs, or pseudopotentials, may further contribute to the discrepancies found between theoretical studies.

Introducing oxygen vacancies into the CaMnO₃ lattice leads to clear structural responses, summarized in **Table 2**. As δ increases from 0 to 0.5, the lattice undergoes distortions that reflect the system's effort to accommodate the removal of oxygen atoms. The a lattice constant expands steadily up to $\delta = 0.25$, followed by a slight contraction at higher vacancy levels. The b lattice constant fluctuates more irregularly, indicating local structural relaxations rather than a uniform expansion or contraction. In contrast, the c lattice constant remains relatively stable at low δ but exhibits a pronounced decrease around $\delta = 0.375$, before expanding again and reaching its maximum value at $\delta = 0.5$.

The lattice angles, ideally 90° in the orthorhombic structure, begin to deviate as vacancies are introduced. These deviations become more pronounced at higher δ , with γ reaching 92.1° at δ = 0.375 and β increasing to 92.3° at δ = 0.5. Such angular distortions indicate a departure from ideal orthorhombic symmetry, most likely associated with octahedral tilting and local strain induced by the vacancies.

Table 2 Lattice parameters of CaMnO_{3-δ}.

δ	0	0.0625	0.125	0.1875	0.25	0.3125	0.375	0.4375	0.5
a (Å)	5.325	5.348	5.375	5.383	5.454	5.431	5.422	5.375	5.392
b (Å)	5.398	5.416	5.429	5.419	5.328	5.400	5.415	5.346	5.382
c (Å)	7.554	7.554	7.561	7.554	7.625	7.650	7.467	7.948	8.026
α (°)	90.0	90.086	90.162	90.0	90.713	90.441	90.0	89.92	90.152
β (°)	90.0	89.949	90.056	90.0	90.0	90.253	90.0	90.12	92.321
γ (°)	90.0	89.657	89.755	90.364	90.004	89.855	92.105	89.569	89.996
$V(Å^3)$	217.11	218.74	220.64	220.33	221.57	224.35	219.08	228.35	232.67

The changes in bond lengths support this interpretation. In stoichiometric CaMnO₃, Mn-O bond lengths are nearly uniform, consistent with undistorted MnO₆ octahedra. With increasing δ , the range between the shortest and longest Mn-O bonds widens significantly, revealing local distortions in the octahedra. The Ca-O bond lengths show similar variability, suggesting that the calcium coordination environment also adjusts to the defect formation. The estimated Mn-

O and Ca-O bond lengths for the supercells are presented in **Table 3**. Additionally, changes in Mn-Mn distances with increasing δ may influence magnetic interactions and contribute to the variations in stability observed in oxygen-deficient structures.

Table 3 Average, minimum, and maximum bond lengths of Mn-O and Ca-O in CaMnO_{3-δ}.

δ	0	0.0625	0.125	0.1875	0.25	0.3125	0.375	0.4375	0.5
Mn-O (Å) (avg)	1.94	1.95	1.95	1.95	1.96	1.97	1.96	1.98	2.02
Mn-O (Å) (min)	1.94	1.90	1.83	1.89	1.90	1.89	1.89	1.88	1.87
Mn-O (Å) (max)	1.95	1.98	2.01	2.01	2.07	2.17	2.15	2.22	2.38
Ca-O (Å) (avg)	2.46	2.48	2.48	2.53	2.54	2.52	2.56	2.57	2.51
Ca-O (Å) (min)	2.32	2.27	2.26	2.26	2.29	2.29	2.29	2.32	2.26
Ca-O (Å) (max)	2.63	2.99	2.99	2.99	2.99	2.99	2.97	2.94	2.88

Overall, the observed structural evolution highlights the complex interplay between lattice relaxation, defect accommodation, and symmetry breaking in CaMnO_{3-δ}. The non-linear trends in lattice parameters and angles emphasize the importance of capturing vacancy effects explicitly in simulations, as they can significantly alter structural properties, which in turn will influence thermal and electronic properties.

4.2 Calculated thermal properties

By applying the method described in the previous section, the coefficients in the expression for the heat capacity in Equation (15) were determined for each oxygen vacancy concentration. The enthalpy of formation and entropy, both at room temperature, were also estimated and are presented in Table 4.

Table 4 Thermodynamic properties of structures with different oxygen vacancy concentrations based on GGA+U calculations.

Caratana	$\Delta_f H^{298.15K}$	$S^{298.15K}$	k_0	\mathbf{k}_1	k_2	k_3	k ₄
System	[kJ/mol]	[J/molK]	[J/molK]	[J/molK ^{0.5}]	[J/mol]	[JK/mol]	[JK ² /mol]
CaMnO _{2.5}	-1.092x10 ⁶	100.03	94.26	4.72x10 ³	-153.19x10 ³	34.28x10 ⁶	-4.06x10 ⁹
CaMnO _{2.5625}	-1.112 x10 ⁶	98.49	19.11	11.47x10 ³	-320.98x10 ³	69.15x10 ⁶	-7.93x10 ⁹
CaMnO _{2.625}	-1.134 x10 ⁶	100.08	48.58	9.37x10 ³	-269.19x10 ³	58.28x10 ⁶	-6.73x10 ⁹
CaMnO _{2.6875}	-1.138 x10 ⁶	97.22	-34.96	16.66x10 ³	-446.74x10 ³	93.99x10 ⁶	-10.60x10 ⁹
CaMnO _{2.75}	-1.149 x10 ⁶	99.55	24.41	11.95x10 ³	-333.78x10 ³	71.49x10 ⁶	-8.18x10 ⁹
CaMnO _{2.8125}	-1.160 x10 ⁶	98.76	-45.48	18.10x10 ³	-481.83x10 ³	100.53x10 ⁶	-11.27x10 ⁹
CaMnO _{2.875}	-1.168 x10 ⁶	95.79	-14.01	15.57x10 ³	-424.29x10 ³	90.14x10 ⁶	-10.24x10 ⁹
CaMnO _{2.9375}	-1.179 x10 ⁶	93.48	-34.61	17.49x10 ³	-471.24x10 ³	99.43x10 ⁶	-11.25x10 ⁹
CaMnO₃	-1.189x10 ⁶	96.32	-46.62	19.18x10 ³	-514.48x10 ³	108.49x10 ⁶	-12.26x10 ⁹

The calculated heat capacities for the different oxygen vacancy concentrations, illustrated in **Figure 5**, show a generally good agreement with values derived from experimental and thermodynamic data in the datasets by Rørmark et al. [36], Bakken et al. [37], and the semi-empirical model of Goldyreva et al. [65]. Although the first-principles results exhibit a somewhat larger spread across compositions, the overall temperature dependence remains consistent with the reference data.

The decrease in heat capacity with increasing oxygen vacancy concentration follows naturally from the reduced number of atoms per formula unit. However, several compositions display distinct local deviations, most notably a sharper rise in Cp around 800 K for certain vacancy configurations. This feature originates from chemical ordering effects, specifically order–disorder transitions that enhance the vibrational contribution to the heat capacity. The transition temperatures vary with defect concentration, which explains why some anomalies appear outside the temperature range depicted in **Figure 5**.

To assess the thermodynamic stability of CaMnO₃, formation enthalpies were evaluated using several exchange-correlation functionals. While GGA+U calculations overestimated the compound's $\Delta_f H^{298.15K}$ by roughly 50 kJ/mol relative to data obtained through FactSage [58], both SCAN and r²SCAN yielded values much closer to the measured reference but still 26

kJ/mol higher relative to the data obtained through thermodynamic calculations with FactSage using the databases FactPS and FTOxid [58]. The improvement observed for the meta-GGA functionals reflects their more balanced treatment of electron localization and hybridization effects, which are critical in mixed-valence oxides such as CaMnO₃.

These trends highlight a broader methodological point: the choice of functional significantly affects computed thermodynamic quantities, particularly in transition-metal oxides, where strong correlation and magnetic ordering play key roles. In this context, SCAN and r²SCAN appear to be a functional more suited to study the material, however this would come at a high computational cost that might be difficult to argue for in a screening of materials.

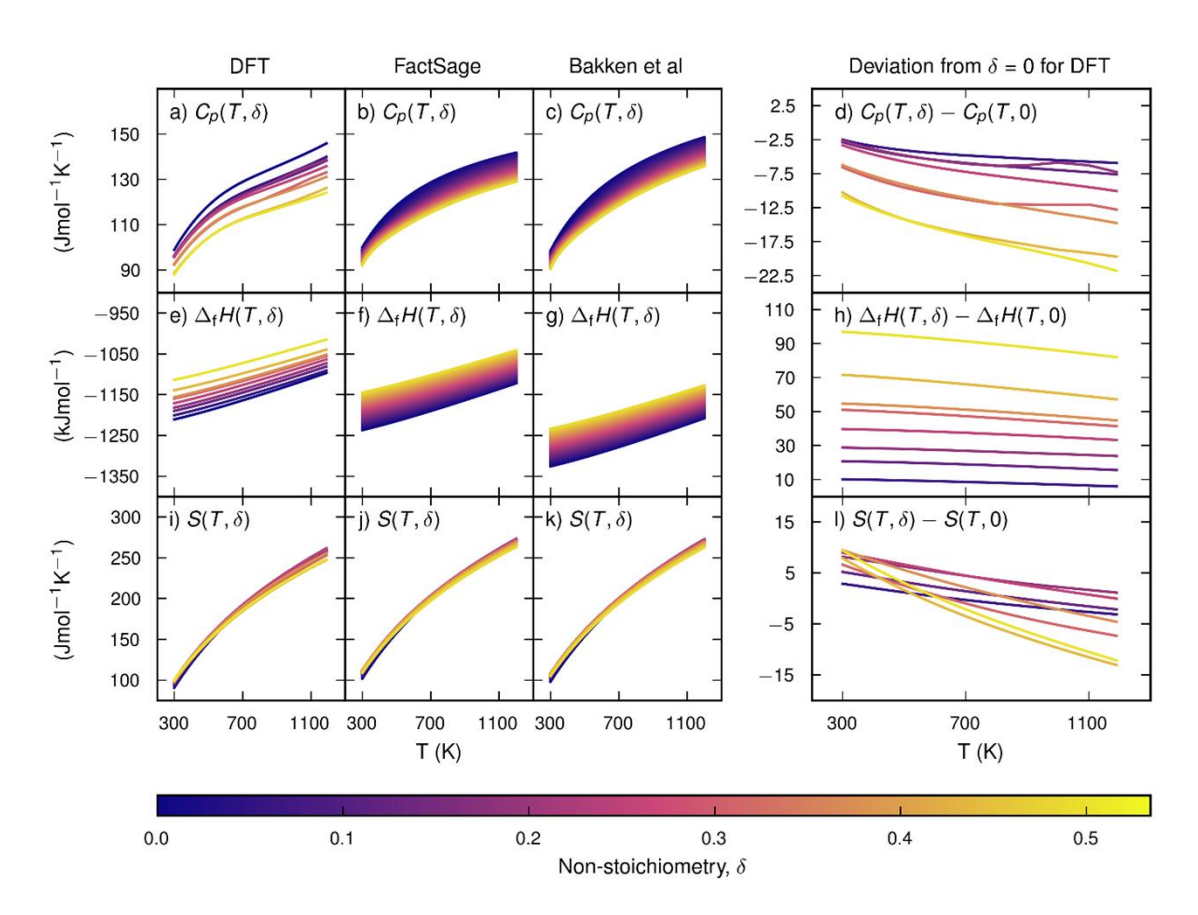


Figure 5 Heat capacity (a-d), formation enthalpy (e-h), and entropy (i-l) from DFT calculations (a, e, i) as well as a semi-empirical model combined with experimental data from either FactSage (b, f, j) or Rørmark et al. and Bakken et al. (c, g, k). The panels in the leftmost column (d, h, l) show the deviation between $\delta = 0$ and $\delta > 0$. Figure from **Paper II**.

It can be concluded that the calculated heat capacity and entropy are well within the experimental margin of error ($\pm 10\%$). The formation enthalpies obtained from first-principles indicate that CaMnO_{3- δ} is significantly less stable compared to the experimental data, however. Even so, it is worth noting that the difference between the results from this study and FactSage

is less than $\pm 10\%$. For comparison with Rørmark et al. and Bakken et al. the difference is close to $\pm 10\%$.

The discrepancy between the computed and experimental formation enthalpies of CaMnO₃ can likely be attributed to a combination of experimental and computational factors. The experimental reference data were derived by combining results from two separate studies [36, 37], where the enthalpy of formation at room temperature was reconstructed from a measurement at 993 K (Rørmark et al. [36]) and a heat capacity dataset extending to 650 K (Bakken et al. [37]). Since CaMnO₃ decomposes above 650 K, the extrapolation to higher temperatures relied on a piecewise cubic Hermite interpolating polynomial (PCHIP), introducing additional uncertainty.

Another possible source of deviation lies in the nature of the experimental samples themselves. The materials reported in these studies may not have been phase-pure CaMnO₃ but rather a mixture of closely related calcium—manganese oxides, potentially containing minor A- or B-site impurities that are not easily detectable in X-ray diffraction patterns. Such structural heterogeneity could yield lower measured formation enthalpies, consistent with the experimental underestimation. Indeed, in chemical-looping experiments involving CaMnO₃, phase diagrams of used materials frequently reveal the presence of secondary phases such as Ca₂MnO₄ or CaMn₂O₄ [22], suggesting that CaMnO₃ may not remain fully stable under operational conditions.

Computational limitations may also contribute to the differences. The finite size of the supercells used to represent the structures necessarily constrains the configurational freedom of the system, which may influence the calculated total energies. Furthermore, the orthorhombic structure considered here represents the most stable phase at 0 K. However, both temperature and oxygen vacancy concentration can induce structural transformations at elevated temperatures [66], which are not explicitly accounted for in DFT. More calculations would be needed to explore this.

4.3 Phase diagram

The thermodynamic data obtained in this work can be combined with the FactSage databases, FTOxid and FactPS, to construct a phase diagram for the Ca-Mn-O system. When using the unadjusted DFT formation enthalpies, the predicted stability of CaMnO_{3-δ} is too low for this phase to appear in the equilibrium diagram. This outcome may not be altogether unexpected, as the calculated formation enthalpy for stoichiometric CaMnO₃ is higher than the

corresponding FactSage value by approximately 26 kJ/mol when using the SCAN or r²SCAN functionals, and by about 48 kJ/mol when using GGA+U, as discussed in the previous section. It should be emphasized that it was not possible to retrieve the underlying thermodynamic data for all components in the Ca-Mn-O system in the FactSage databases, and it is possible that the phase diagram has been empirically optimized to look better in the database.

To address this systematic discrepancy, the calculated formation enthalpies were shifted by the difference between the DFT-derived and FactSage reference values for CaMnO₃ at 298.15 K. The adjusted values were then combined with thermochemical data for other relevant phases obtained from the FactPS and FToxid databases to generate a more consistent phase diagram. The resulting diagram, shown in **Figure 6**, reveals the phase stability regions of CaMnO_{3- δ} under varying temperatures and oxygen partial pressures. The results indicate that the most thermodynamically stable composition transitions from $\delta = 0$ to $\delta = 0.375$ with increasing temperature under oxygen-lean conditions, consistent with the redox behaviour expected in a CLC environment.

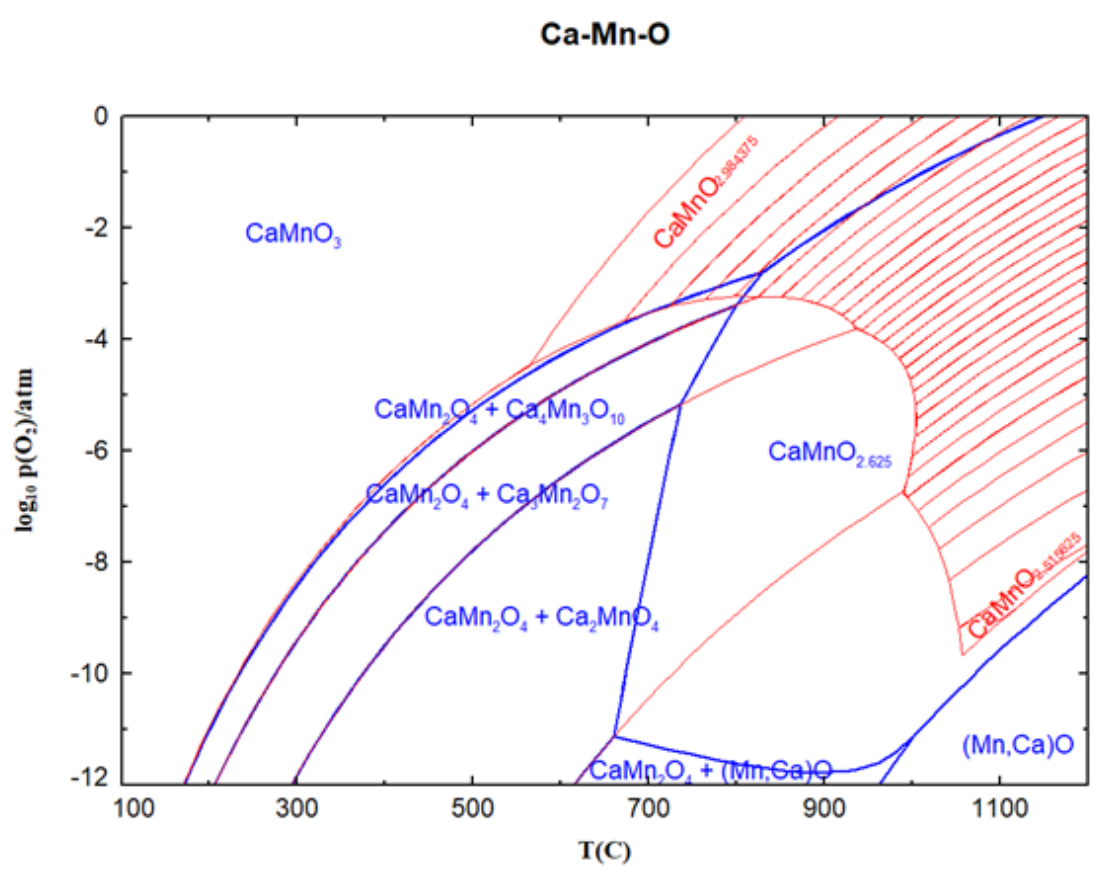


Figure 6 Phase diagram of Ca-Mn-O system, including results from calculations for CaMnO_{3-δ}, which have been adjusted to fit the formation of enthalpy for CaMnO₃ at 298.15 K from the FactSage database, with oxygen vacancies and where data from a semi-empirical model has been superimposed (red lines). Figure from **Paper II**.

This approach demonstrates the potential of using DFT-derived thermodynamic data, corrected through reference databases, to enhance the understanding of material stability under operationally relevant conditions. In practical CLC systems, oxygen carriers must reversibly release and absorb oxygen without decomposing into undesired phases. The constructed phase diagrams therefore provide valuable insight into the thermal stability and phase behaviour of $CaMnO_{3-\delta}$ and help identify compositions that can sustain structural integrity and performance during repeated redox cycling.

For comparison, **Figure 6** also includes predictions based on the semi-empirical model proposed by Goldyreva et al. [65] (red lines). Notably, significant discrepancies are observed between the present results and those obtained with the semi-empirical model. However, it is not immediately clear which dataset most accurately represents the experimental reality. It is also important to emphasize that the phase diagram depicts only the thermodynamically stable phases at equilibrium conditions. Many intermediate oxygen vacancy concentrations are likely metastable rather than globally stable, a feature that may not be fully captured by semi-empirical approaches.

Furthermore, the limited number of oxygen vacancy concentrations explored in this work, eight distinct δ values, introduces some granularity into the analysis. This constraint arises from the computational cost of DFT calculations for large supercells containing more than 80 atoms. A finer sampling of δ values, enabled by larger unit cells or machine learning–accelerated approaches, could provide a clearer picture of the phase evolution and transition boundaries.

The methodology developed here, integrating first-principles thermodynamic predictions with database-driven phase equilibria, represents an important step forward. It enables the exploration of complex oxygen-deficient materials relevant to CLC, allowing the prediction of phase stability and defect-driven behaviour in systems that are difficult or even impossible to probe experimentally. This framework thus offers a pathway for accelerated discovery and optimization of oxygen carriers based on their intrinsic thermodynamic properties.

4.4 Band Structure

The electronic band structures and total densities of states (DOS) were calculated for stoichiometric CaMnO₃ and a series of oxygen-deficient configurations, CaMnO_{3- δ}, with δ ranging from 0.0625 to 0.5. These calculations were performed to investigate how oxygen vacancies influence the electronic properties of the material, particularly the evolution of the band gap and the redistribution of electronic states.

For stoichiometric CaMnO₃, the band structure exhibits a direct band gap of approximately 1.8 eV at the Γ-point, as shown in **Figure 7**. This value is consistent with both experimental estimates, which range from 1.0 to 3.6 eV [64, 67, 68], and earlier DFT studies reporting band gaps between 0.5 and 3.0 eV depending on the exchange–correlation functional and computational parameters used [41, 42, 69, 70]. Such a gap places CaMnO₃ within the semiconducting regime.

The introduction of oxygen vacancies has a pronounced effect on the electronic structure. As δ increases, the band gap narrows and eventually closes, as illustrated in **Figure 8**. At δ = 0.0625, the gap becomes indirect and decreases to about 0.9 eV. For δ = 0.125, it narrows further to roughly 0.4 eV, and by δ = 0.1875 the material exhibits metallic behaviour, with the valence and conduction bands overlapping at the Fermi level. Interestingly, further increases in vacancy concentration led to a re-opening of the gap at certain compositions, suggesting that the electronic response to oxygen deficiency is not monotonic. This non-linear evolution is likely linked to local lattice distortions and changes in orbital hybridization introduced by the vacancies.

The total DOS plots complement the band structures by showing how the oxygen deficiency affects the distribution of electronic states near the Fermi level. With increasing δ , defect-induced states emerge within the original band gap and progressively shift toward the Fermi level. For δ values around 0.375–0.5, the Fermi level intersects these defect states, giving rise to semi-metallic or metallic behaviour. The increase in DOS at the Fermi level indicates enhanced electronic conductivity and suggests that oxygen vacancies effectively act as electron donors.

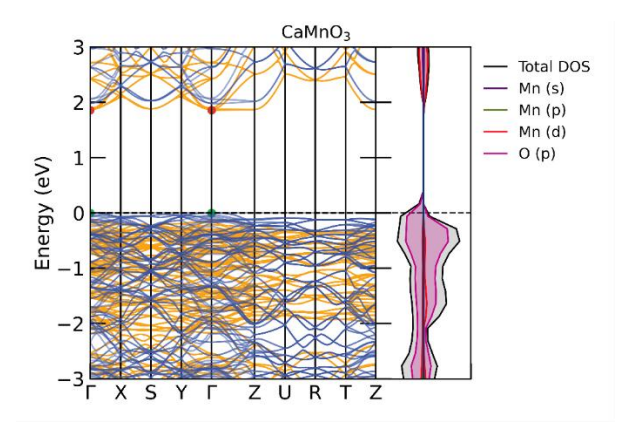


Figure 7 Band structure and DOS-plot for stoichiometric CaMnO₃. Orange bands represent spin-up and blue spin-down, while the red dot is the lowest point of the conduction bands and the green dot is the highest point of the valence band. Figure from **Paper III**.

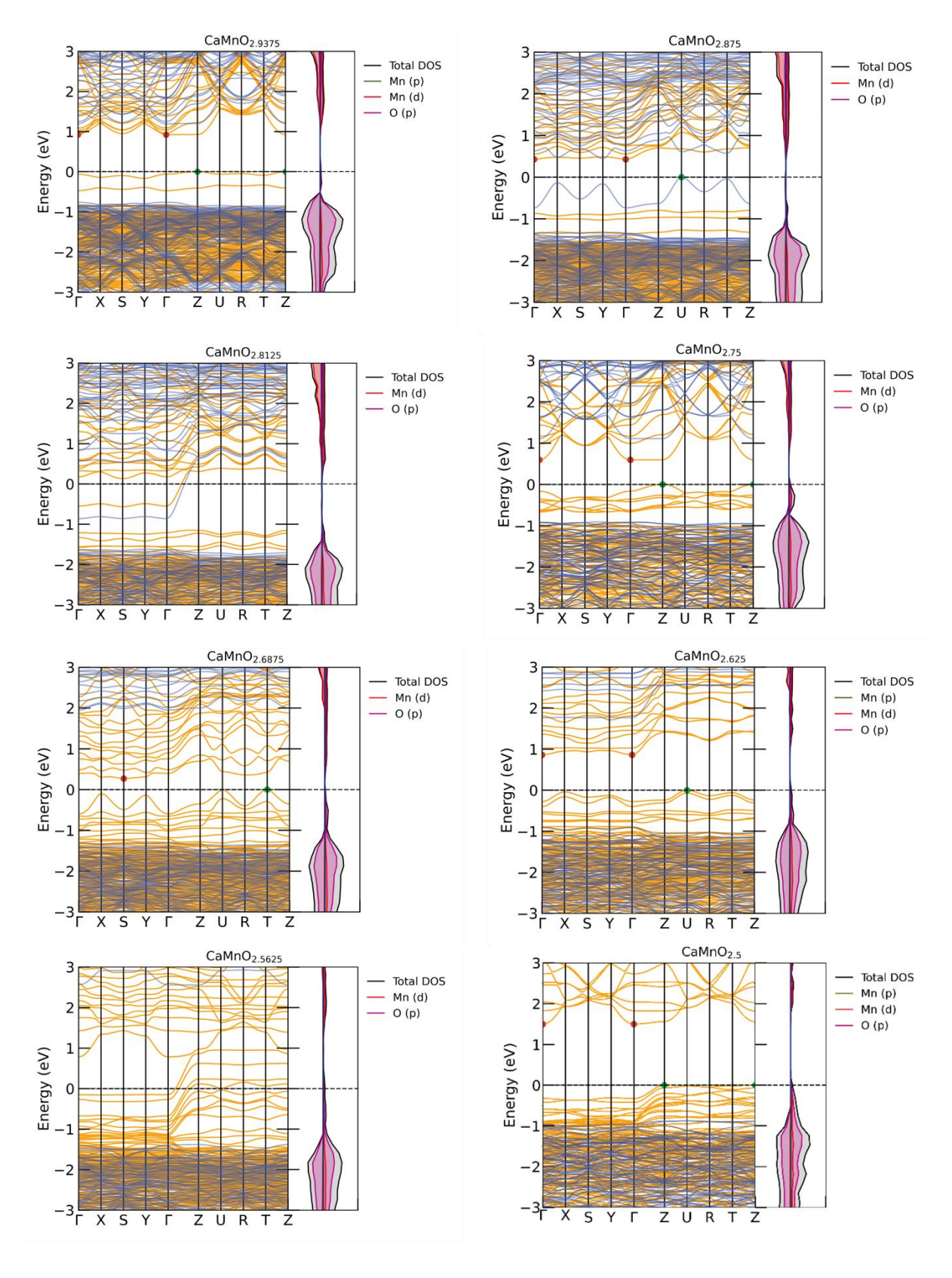


Figure 8 Band structure and DOS for CaMnO_{3- δ}. The orange lines represent spin-up and blue spin-down, while the red dot is the lowest point of the conduction bands and the green dot is the highest point of the valence bands. Figure from **Paper III**.

The redistribution of charge in response to oxygen deficiency was further analysed through Bader charge calculations. The results reveal systematic trends in the average charges of Ca, Mn, and O as a function of the vacancy concentration δ , as shown in **Table 5**.

Table 5 Average Bader charges of CaMnO_{3-δ}.

δ	0	0.0625	0.125	0.1875	0.25	0.3125	0.375	0.4375	0.5
Ca (e)	1.674	1.674	1.673	1.672	1.668	1.667	1.667	1.666	1.660
Mn (e)	2.240	2.204	2.170	2.133	2.113	2.068	2.033	2.007	1.976
O (e)	-1.305	-1.320	-1.337	-1.353	-1.375	-1.390	-1.410	-1.434	-1.455

For stoichiometric CaMnO₃ ($\delta = 0$), the average Bader charges are approximately +1.674 e for Ca, +2.240 e for Mn, and -1.305 e for O. With increasing δ , the Mn charge decreases steadily, reaching +1.976 e at $\delta = 0.5$. This reduction reflects the progressive change in oxidation state from Mn⁴⁺ toward Mn³⁺, consistent with the expected localization of excess electrons introduced by oxygen removal.

The oxygen atoms, in contrast, exhibit increasingly negative charges, shifting from -1.305 e to about -1.455 e as δ increases. This trend suggests that the remaining oxygen ions accommodate a larger fraction of the electron density released by the removed oxygen atoms. The Ca ions show only a minor decrease in average charge, indicating that they remain largely as they were and are inert with respect to the vacancy-induced changes.

The combined evolution of Bader charges highlights a cooperative response of the lattice: electrons left behind by the missing oxygen atoms localize primarily on nearby Mn cations, reducing them, while partial charge redistribution also affects neighbouring O sites. This mechanism emphasizes the observed modification of the band structure and explains the correlation between increasing δ and enhanced electronic conductivity.

Overall, these results demonstrate that oxygen vacancies play a key role in controlling the electronic character of CaMnO_{3-δ}. The progressive narrowing of the band gap, the emergence of defect states, and the associated charge redistribution collectively indicate a transition from semiconducting to metallic behaviour. Such tunability highlights the potential of oxygen-deficient CaMnO₃ as a functional material in applications requiring adjustable electronic conductivity, such as in thermochemical or catalytic processes where redox flexibility is advantageous.

4.5 Oxygen Vacancy formation

The formation energies of oxygen vacancies in CaMnO₃ were calculated for vacancy concentrations (δ) ranging from 0 to 0.5. The results, summarized in **Table 6**, exhibit a distinctly nonlinear relationship between vacancy formation energy and δ , reflecting an increasing energetic cost associated with the removal of additional oxygen atoms. This behaviour can be divided into three regimes corresponding to low (δ = 0.0625–0.1875), intermediate (δ = 0.25–0.375), and high (δ = 0.4375–0.5) vacancy concentrations.

Table 6 Oxygen vacancy formation energies per oxygen vacancy at 0 K.

δ	0	0.0625	0.125	0.1875	0.25	0.3125	0.375	0.4375	0.5
$E_{V_0}(eV)$	-	2.03	2.01	1.83	1.89	1.95	1.75	1.95	2.26

At low vacancy concentrations, the formation energy remains relatively constant, close to 2 eV per oxygen atom. This suggests that the perovskite structure of CaMnO₃ can initially accommodate oxygen vacancies without severe energetic penalties, likely due to local lattice relaxations and the inherent defect tolerance of the crystal. Nevertheless, these values are comparatively high, implying that spontaneous vacancy formation is thermodynamically unfavourable under standard conditions. This observation is consistent with earlier computational studies [71]. It should also be noted that the data presented here correspond to 0 K, meaning that finite-temperature effects such as lattice vibrations and configurational entropy could reduce the effective vacancy formation energy at elevated temperatures.

In the intermediate range (δ = 0.25–0.375), the formation energy per oxygen atom decreases, reaching values between 1.83 and 1.95 eV. The lowest formation energy is observed at δ = 0.375, where the value drops to 1.75 eV. This reduction suggests that, within this concentration range, the formation of additional vacancies may become slightly more favourable. Such a trend could be associated with the stabilization of certain local arrangements of oxygen vacancies, which may lead to ordered or partially ordered defect configurations that minimize strain energy within the lattice.

At higher vacancy concentrations ($\delta \ge 0.4375$), the formation energy increases sharply to 2.26 eV per oxygen atom. This pronounced rise indicates that the system is approaching its limit of structural stability. Beyond this concentration, the perovskite lattice likely experiences substantial distortion or begins to transform toward competing phases such as Ruddlesden–

Popper–type structures or other manganese oxides, which have been observed in experimental and theoretical studies. The nonlinear dependence of vacancy formation energy on δ thus reflects the competition between defect-induced stabilization at moderate vacancy levels and destabilization due to lattice distortion and phase separation at higher δ .

Overall, these results underscore the importance of considering vacancy concentration when evaluating the thermodynamic stability and redox behaviour of oxygen-deficient CaMnO₃. Low levels of oxygen deficiency appear to be thermodynamically accessible, whereas higher vacancy concentrations likely require non-equilibrium synthesis routes or are only stabilized under reducing conditions relevant to CLC operation. The local minimum in vacancy formation energy at $\delta = 0.375$ further suggests that this composition may represent a particularly stable nonstoichiometric phase, in agreement with experimental observations of phase transitions occurring near similar oxygen deficiency levels [63].

4.6 Powder X-ray Diffraction

To further validate the structural models obtained from DFT calculations, powder X-ray diffraction (PXRD) patterns were simulated for each relaxed CaMnO_{3-δ} structure using the VESTA software [72]. These simulated diffraction patterns act as theoretical fingerprints of the predicted structures and enable a qualitative comparison with experimental observations reported in the literature. PXRD is a key technique for phase identification and has been widely used to characterize CaMnO₃ and related perovskite oxides. By comparing simulated PXRD patterns across different oxygen vacancy concentrations, it is possible to evaluate whether the structural changes introduced by vacancies are sufficiently pronounced to be experimentally detectable.

PXRD patterns were simulated based on the relaxed CaMnO_{3-δ} structures using a radiation wavelength of 1.5406 Å, corresponding to Cu Kα. The simulated PXRD pattern for stoichiometric CaMnO₃, shown in **Figure 9**, reproduces the characteristic features reported in experimental studies, most notably the positions and relative intensities of the principal reflections [73-77]. In particular, the dominant peaks near $2\Theta \approx 34^\circ$, 48° , and 59° closely match experimental peaks at approximately 34° , 48° , and 60° , consistent with the orthorhombic perovskite structure (Pnma). This agreement indicates that the DFT-relaxed structure provides a physically realistic basis for further analysis and serves as a reliable reference for comparison with the simulated PXRD patterns of oxygen-deficient compositions.

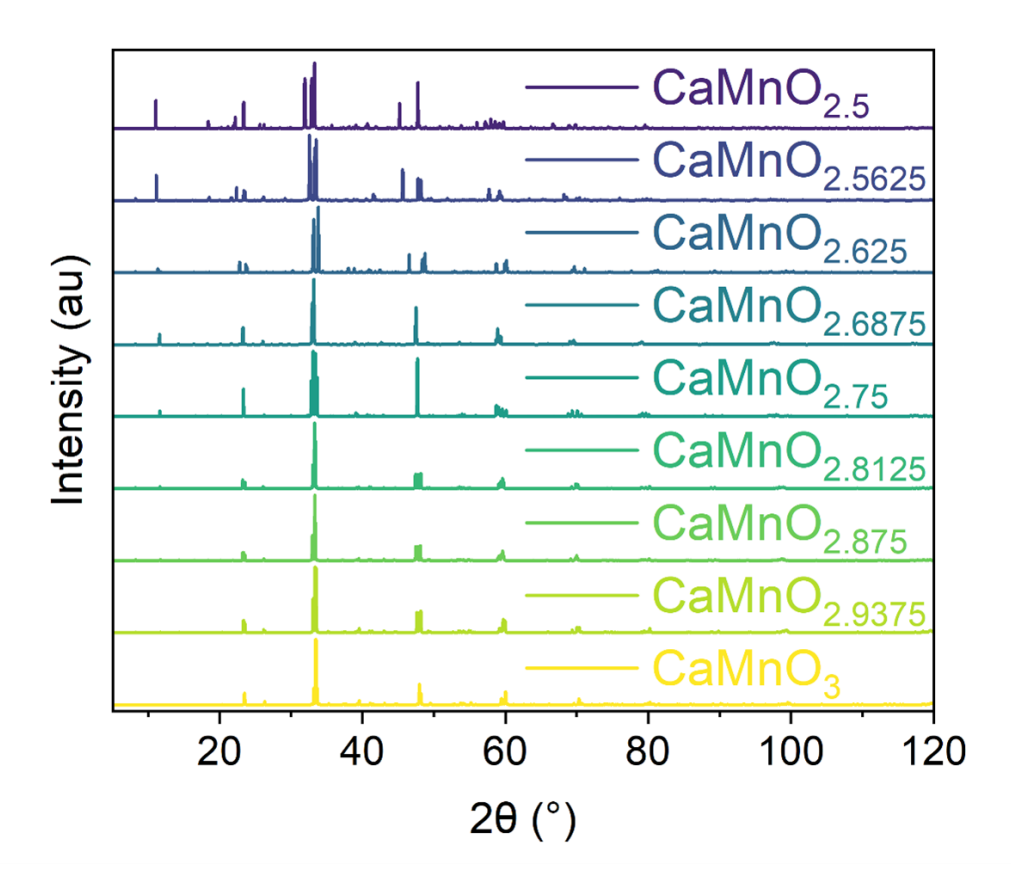


Figure 9 Simulated PXRD patterns of CaMnO_{3- δ} structures generated from DFT-optimized geometries using VESTA and Cu K α radiation ($\lambda = 1.5406$ Å). The comparison illustrates how oxygen vacancies affect the positions and intensities of the main diffraction peaks, indicating symmetry distortions at higher vacancy concentrations.

At low oxygen vacancy concentrations, the PXRD patterns remain largely unchanged relative to the stoichiometric case, suggesting that the crystal structure is resilient to small deviations from ideal stoichiometry. However, at $\delta=0.375$, a noticeable change appears: the peaks near 34° and 48° begin to split, indicating a structural distortion significant enough to be experimentally observed. A similar but weaker effect may also occur for the 60° peak, though its lower intensity makes the interpretation less certain. These splits persist at higher vacancy levels, signifying progressive lattice distortions or symmetry reductions as oxygen vacancies accumulate.

Comparable observations have been reported by Poeppelmeier et al. [63] for $\delta = 0.5$, but the present results suggest that these structural changes may begin at considerably lower oxygen vacancy concentrations. Further investigation using larger simulation cells and higher-resolution PXRD models could provide more detailed insight into the precise onset of this transition, though such studies would come at a significantly higher computational cost.

Caution is warranted when interpreting experimental PXRD data for CaMnO₃ and similar perovskites, as subtle peak shifts or splits can lead to misidentification of phases. For instance, CaMnO₃ is known to decompose into related phases such as Ca₂MnO₄, CaMn₂O₄, and Ca₃Mn₂O₇ at elevated temperatures [73-78]. The simulated PXRD patterns for non-stoichiometric CaMnO₃ also show similarities to these phases, particularly in the appearance of double peaks in the 30-35° and 45-50° ranges. This resemblance suggests a possible structural convergence or phase transition pathway, underscoring the complex structural behaviour of CaMnO_{3-δ} under oxygen-deficient conditions.

5 Conclusions

The work presented in this thesis contributes to the growing field of computational materials research for chemical-looping applications by establishing a systematic first-principles framework for evaluating oxygen carrier materials. While earlier studies of oxygen carriers have primarily focused on experimental characterization or semi-empirical thermodynamic modelling, the present work extends the use of DFT to capture structural, electronic, and thermodynamic properties within a single, consistent approach. Through detailed modelling of oxygen vacancies, the methodology developed here enables the prediction of redox behaviour and defect energetics under conditions relevant to chemical looping. In doing so, it provides new insights into the fundamental mechanisms that govern the stability and performance of perovskite-based oxygen carriers such as CaMnO_{3-δ}.

The structural analysis confirmed that the DFT-optimized lattice parameters of stoichiometric $CaMnO_3$ are in close agreement with both experimental and previous theoretical data, with deviations consistent with the known tendencies of the GGA+U functional. Upon introducing oxygen vacancies, the lattice undergoes distortions and symmetry-breaking effects, primarily associated with octahedral tilting and local relaxation around the defect sites. These distortions increase nonlinearly with δ and are accompanied by a widening distribution of Mn-O and CaO bond lengths, reflecting enhanced structural flexibility at higher vacancy concentrations.

Such lattice responses to oxygen deficiency provide an important foundation for understanding the concurrent changes in electronic and thermodynamic properties, emphasizing the close coupling between structure, defects, and functionality in CaMnO_{3-δ}.

The assessment of formation enthalpies across different exchange–correlation functionals demonstrated that meta-GGA approaches (SCAN, r²SCAN) provide significantly improved agreement with experimental thermochemical data compared to GGA+U. This improvement underscores the importance of accurate treatment of electron localization in perovskite-type oxides. Overall, the study shows that advanced computational methods can be reliably applied to predict thermodynamic stability trends in oxygen carrier materials, paving the way for computational screening of new candidates.

The comparison between calculated and experimental formation enthalpies indicates that the remaining discrepancies could be explained by uncertainties in the experimental reference data

and intrinsic modelling limitations. The combined use of datasets measured at different temperatures and extrapolated beyond the stability range of CaMnO₃ introduces uncertainty on the experimental side, while the static DFT approach and finite supercell sizes limit the accuracy of the computed energetics. Moreover, the possible presence of secondary phases in experimental samples suggests that pristine CaMnO₃ may represent a thermodynamically complex mixture. These observations underline the need for both improved experimental characterization and more advanced modelling approaches that capture temperature-dependent and configurational effects.

Comparison between the calculated and experimentally derived heat capacities demonstrates that the present DFT approach captures both the general temperature dependence and the magnitude of the heat capacity across varying oxygen vacancy concentrations in CaMnO_{3-δ}. The observed order–disorder transitions highlight how local chemical configurations influence thermodynamic behaviour, emphasizing the importance of accounting for configurational effects when modelling defect-rich oxides.

The analysis of the electronic band structure and density of states reveals that oxygen vacancies have a pronounced effect on the electronic behaviour of CaMnO_{3- δ}. The progressive reduction of the bandgap with increasing δ , followed by gap reopening at higher vacancy concentrations, reflects a complex interplay between defect formation, local lattice distortions, and charge redistribution. These effects are verified by the Bader charge analysis, which shows a systematic reduction of Mn oxidation states and a corresponding increase in electron localization near the defect sites. The observed transition from semiconducting to metallic-like behaviour at intermediate δ values highlights the tunability of the electronic structure through controlled defect engineering. These findings emphasize that nonstoichiometric oxygen not only modifies the electronic conductivity but also underpins the thermodynamic and redox properties central to CaMnO_{3- δ}'s function as an oxygen carrier.

The analysis of oxygen vacancy formation energies provides important insight into the redox behaviour and thermodynamic stability of CaMnO_{3- δ} as an oxygen carrier. The results indicate that oxygen vacancies are energetically accessible only up to moderate concentrations, while higher levels of oxygen deficiency become increasingly unfavourable. This suggests that CaMnO₃ can undergo reversible oxygen release and uptake within a limited δ range, which is consistent with the requirements for efficient operation in chemical looping combustion. The local stability minimum identified near δ = 0.375 aligns with experimental evidence for phase

transitions occurring at similar compositions, highlighting this concentration as a particularly promising regime for stable redox cycling. These findings reinforce the view that understanding and controlling oxygen vacancy formation is essential for optimizing both the thermodynamic and kinetic properties of perovskite-based oxygen carriers.

The simulated PXRD patterns provided valuable confirmation of the accuracy and reliability of the DFT-optimized structures of CaMnO_{3-δ}. The close agreement between the simulated and experimental patterns for stoichiometric CaMnO₃ confirms that the orthorhombic perovskite structure (Pnma) was correctly reproduced in this work, thereby supporting the validity of the computational framework used throughout the study.

As the oxygen vacancy concentration increased, systematic peak shifts and splits were observed, particularly near $\delta=0.375$. These diffraction signatures point to progressive structural distortions that may precede phase transitions or symmetry lowering in oxygen-deficient compositions. The onset of such changes at relatively low vacancy concentrations indicates that the perovskite lattice is sensitive to defect formation, which could have implications for the material's thermal and chemical stability under cyclic redox conditions.

The PXRD simulations also reveal how subtle structural rearrangements in CaMnO_{3-δ} can produce patterns resembling those of known decomposition products, such as Ca₂MnO₄ or Ca₃Mn₂O₇. This highlights the importance of careful experimental interpretation when characterizing oxygen-deficient or partially reduced CaMnO₃ samples. Overall, the simulated PXRD results strengthen the connection between atomic-level vacancy effects and experimentally observable diffraction features, demonstrating how DFT-based modelling can complement and guide phase identification in the development of oxygen carrier materials.

6 Future work

While the methods used in this thesis demonstrate the capability of DFT to predict the thermodynamic and electronic properties of oxygen carriers such as CaMnO_{3-δ}, further studies are required to close the gap between computational and experimental observations. The observed discrepancies between theoretical and measured formation enthalpies, in particular, merit deeper investigation.

One promising direction is the exploration of doped variants of CaMnO₃, where the substitution of elements on the A- or B-site in the perovskite could modify electronic structure, stability, and oxygen transport properties. The computational framework developed in this work can be readily extended to study such doped systems, offering insight into how elemental substitution influences defect formation, phase stability, and redox behaviour. Similarly, the role of extended defects, such as grain boundaries, should be examined, as they are known to significantly affect the stability and reactivity of perovskite oxides under operating conditions.

Beyond DFT, there is also a need to address the computational limitations that arise when modelling complex systems at realistic length and time scales. Machine learning potentials (MLPs) represent a promising approach for bridging this gap. By training neural network-based potentials on DFT data, it is possible to perform large-scale molecular dynamics simulations with near first-principles accuracy but at a fraction of the computational cost. This would enable simulations involving much larger supercells and longer time scales, providing new opportunities to study diffusion mechanisms, defect migration, and temperature-dependent phenomena in CaMnO_{3-δ} and related oxygen carrier materials.

Together, these approaches; chemical doping, defect modelling, and machine learning-accelerated simulations, form a natural continuation of the present work and could lead to a more complete understanding of the structural, thermodynamic, and kinetic properties that govern oxygen carrier performance.

- [1] R. E. Hummel, *Understanding materials science History, Properties, Applications*. New York, NY: Springer New York, 1998.
- [2] N. Hirota, *A history of modern chemistry*. Apollo Books, 2016.
- [3] J. Evans and A. S. Thorndike, *Quantum mechanics at the crossroads: New perspectives from history, philosophy and physics.* Springer Science & Business Media, 2006.
- [4] S. Luo, T. Li, X. Wang, M. Faizan, and L. Zhang, "High-throughput computational materials screening and discovery of optoelectronic semiconductors," *Wiley Interdisciplinary Reviews: Computational Molecular Science*, vol. 11, no. 1, p. e1489, 2021.
- [5] Y. Yan, T. Mattisson, P. Moldenhauer, E. J. Anthony, and P. T. Clough, "Applying machine learning algorithms in estimating the performance of heterogeneous, multi-component materials as oxygen carriers for chemical-looping processes," *Chemical Engineering Journal*, vol. 387, p. 124072, 2020.
- [6] X. Zhang, A. Chen, and Z. Zhou, "High-throughput computational screening of layered and two-dimensional materials," *Wiley Interdisciplinary Reviews: Computational Molecular Science*, vol. 9, no. 1, p. e1385, 2019.
- [7] M. Almalki, N. Lachiche, and Y. A. Chapuis, "Active learning concept for materials process optimization of non-fullerene organic photovoltaic using small datasets," in *Data Science for Photonics and Biophotonics*, 2024, vol. 13011: SPIE, pp. 36-50.
- [8] U. Nwabara *et al.*, "High throughput computational and experimental methods for accelerated electrochemical materials discovery," *Journal of Materials Chemistry A*, 2025.
- [9] C. A. Mirkin, E. H. Sargent, and D. P. Schrag, "Energy transition needs new materials," *Science*, vol. 384, no. 6697, pp. 713-713, 2024.
- [10] G. A. Ozin and J. Y. Loh, *Energy Materials Discovery: Enabling a Sustainable Future*. Royal Society of Chemistry, 2022.
- [11] A. Y. S. Eng *et al.*, "Theory-guided experimental design in battery materials research," *Science Advances*, vol. 8, no. 19, p. eabm2422, 2022.
- [12] M. Lu *et al.*, "Covalent organic framework based functional materials: important catalysts for efficient CO2 utilization," *Angewandte Chemie*, vol. 134, no. 15, p. e202200003, 2022.
- [13] Y. Sun and S. Dai, "High-entropy materials for catalysis: A new frontier," *Science advances*, vol. 7, no. 20, p. eabg1600, 2021.
- [14] K. Sivula and R. Van De Krol, "Semiconducting materials for photoelectrochemical energy conversion," *Nature Reviews Materials*, vol. 1, no. 2, pp. 1-16, 2016.
- [15] S. G. Louie, Y.-H. Chan, F. H. da Jornada, Z. Li, and D. Y. Qiu, "Discovering and understanding materials through computation," *Nature Materials*, vol. 20, no. 6, pp. 728-735, 2021.
- [16] K. Shahzad, A. I. Mardare, and A. W. Hassel, "Accelerating materials discovery: combinatorial synthesis, high-throughput characterization, and computational advances," *Science and Technology of Advanced Materials: Methods*, vol. 4, no. 1, p. 2292486, 2024.
- [17] C. Duan, A. Nandy, and H. J. Kulik, "Machine learning for the discovery, design, and engineering of materials," *Annual Review of Chemical and Biomolecular Engineering*, vol. 13, no. 1, pp. 405-429, 2022.

- [18] A. Lyngfelt, B. Leckner, and T. Mattisson, "A fluidized-bed combustion process with inherent CO2 separation; application of chemical-looping combustion," *Chemical Engineering Science*, vol. 56, no. 10, pp. 3101-3113, 2001.
- [19] J. Adánez and A. Abad, "Chemical-looping combustion: Status and research needs," *Proceedings of the Combustion Institute*, vol. 37, no. 4, pp. 4303-4317, 2019.
- [20] J. Adanez, A. Abad, F. Garcia-Labiano, P. Gayan, and L. F. De Diego, "Progress in chemical-looping combustion and reforming technologies," *Progress in energy and combustion science*, vol. 38, no. 2, pp. 215-282, 2012.
- [21] T. Mattisson and A. Lyngfelt, "Applications of chemical-looping combustion with capture of CO2," *Second nordic minisymposium on CO2 capture and storage, Göteborg, Sweden,* 2001.
- [22] T. Mattisson, "Materials for chemical-looping with oxygen uncoupling," *International Scholarly Research Notices*, vol. 2013, no. 1, p. 526375, 2013.
- [23] H. Leion, A. Lyngfelt, M. Johansson, E. Jerndal, and T. Mattisson, "The use of ilmenite as an oxygen carrier in chemical-looping combustion," *Chemical engineering research and design*, vol. 86, no. 9, pp. 1017-1026, 2008.
- [24] T. Mattisson, M. Johansson, and A. Lyngfelt, "The use of NiO as an oxygen carrier in chemical-looping combustion," *Fuel*, vol. 85, no. 5-6, pp. 736-747, 2006.
- [25] M. Rydén, D. Jing, M. Kallen, H. Leion, A. Lyngfelt, and T. Mattisson, "CuO-based oxygen-carrier particles for chemical-looping with oxygen uncoupling—experiments in batch reactor and in continuous operation," *Industrial & Engineering Chemistry Research*, vol. 53, no. 15, pp. 6255-6267, 2014.
- [26] M. Arjmand, H. Leion, T. Mattisson, and A. Lyngfelt, "Investigation of different manganese ores as oxygen carriers in chemical-looping combustion (CLC) for solid fuels," *Applied Energy*, vol. 113, pp. 1883-1894, 2014.
- [27] C. Linderholm, A. Lyngfelt, A. Cuadrat, and E. Jerndal, "Chemical-looping combustion of solid fuels—Operation in a 10 kW unit with two fuels, above-bed and in-bed fuel feed and two oxygen carriers, manganese ore and ilmenite," *Fuel*, vol. 102, pp. 808-822, 2012.
- [28] M. Rydén, H. Leion, T. Mattisson, and A. Lyngfelt, "Combined oxides as oxygen-carrier material for chemical-looping with oxygen uncoupling," *Applied Energy*, vol. 113, pp. 1924-1932, 2014.
- [29] A. Shulman, E. Cleverstam, T. Mattisson, and A. Lyngfelt, "Manganese/iron, manganese/nickel, and manganese/silicon oxides used in chemical-looping with oxygen uncoupling (CLOU) for combustion of methane," *Energy & Fuels*, vol. 23, no. 10, pp. 5269-5275, 2009.
- [30] X. Wang, T. Xu, S. Liu, B. Xiao, Z. Hu, and Z. Chen, "CuO supported on manganese ore as an oxygen carrier for chemical looping with oxygen uncoupling (CLOU)," *Chemical Engineering Journal*, vol. 343, pp. 340-350, 2018.
- [31] Y. Chen, N. Galinsky, Z. Wang, and F. Li, "Investigation of perovskite supported composite oxides for chemical looping conversion of syngas," *Fuel*, vol. 134, pp. 521-530, 2014.
- [32] X. P. Dai, J. Li, J. T. Fan, W. S. Wei, and J. Xu, "Synthesis gas generation by chemical-looping reforming in a circulating fluidized bed reactor using perovskite LaFeO3-based oxygen carriers," *Industrial & engineering chemistry research*, vol. 51, no. 34, pp. 11072-11082, 2012.
- [33] P. Hallberg, D. Jing, M. Rydén, T. Mattisson, and A. Lyngfelt, "Chemical Looping Combustion and Chemical Looping with Oxygen Uncoupling Experiments in a Batch Reactor Using Spray-Dried CaMn1–x M x O3–δ (M= Ti, Fe, Mg) Particles as Oxygen Carriers," *Energy & Fuels*, vol. 27, no. 3, pp. 1473-1481, 2013.

- [34] M. Rydén, A. Lyngfelt, and T. Mattisson, "CaMn0. 875Ti0. 125O3 as oxygen carrier for chemical-looping combustion with oxygen uncoupling (CLOU)—Experiments in a continuously operating fluidized-bed reactor system," *International Journal of Greenhouse gas control*, vol. 5, no. 2, pp. 356-366, 2011.
- [35] J. Brorsson, I. Staničić, J. Gastaldi, T. Mattison, and A. Hellman, "Thermodynamic properties for metal oxides from first-principles," *Computational Materials Science*, vol. 233, p. 112690, 2024.
- [36] L. Rørmark, A. B. Mørch, K. Wiik, S. Stølen, and T. Grande, "Enthalpies of oxidation of CaMnO3-δ, Ca2MnO4-δ and SrMnO3-δ deduced redox properties," *Chemistry of materials*, vol. 13, no. 11, pp. 4005-4013, 2001.
- [37] E. Bakken, T. Norby, and S. Stølen, "Nonstoichiometry and reductive decomposition of CaMnO3– δ," *Solid State Ionics*, vol. 176, no. 1-2, pp. 217-223, 2005.
- [38] B. Grimm and T. Bredow, "Oxygen Defect Formation Thermodynamics of CaMnO3: A Closer Look," *Physica Status Solidi (b)*, vol. 260, no. 1, p. 2200427, 2023.
- [39] B. Grimm and T. Bredow, "Theoretical Study on Proton Migration on the CaMnO3 Surface," *The Journal of Physical Chemistry C*, vol. 128, no. 31, pp. 12792-12798, 2024.
- [40] B. Grimm and T. Bredow, "Revisiting CaMnO3 as a Proton Conductor— A Theoretical Perspective," *The Journal of Physical Chemistry C*, vol. 128, no. 13, pp. 5429-5435, 2024.
- [41] M. Molinari, D. A. Tompsett, S. C. Parker, F. Azough, and R. Freer, "Structural, electronic and thermoelectric behaviour of CaMnO 3 and CaMnO (3–δ)," *Journal of Materials Chemistry A*, vol. 2, no. 34, pp. 14109-14117, 2014.
- [42] F. Zhang, Q. Lu, X. Zhang, and J. Zhang, "First principle investigation of electronic structure of CaMnO3 thermoelectric compound oxide," *Journal of Alloys and Compounds*, vol. 509, no. 2, pp. 542-545, 2011.
- [43] P. Hohenberg and W. Kohn, "Inhomogeneous electron gas," *Physical review*, vol. 136, no. 3B, p. B864, 1964.
- [44] W. Kohn and L. J. Sham, "Self-consistent equations including exchange and correlation effects," *Physical review*, vol. 140, no. 4A, p. A1133, 1965.
- [45] J. P. Perdew, "Climbing the ladder of density functional approximations," *MRS bulletin*, vol. 38, no. 9, pp. 743-750, 2013.
- [46] G. Kresse and J. Furthmüller, "Efficient iterative schemes for ab initio total-energy calculations using a plane-wave basis set," *Physical review B*, vol. 54, no. 16, p. 11169, 1996.
- [47] S. P. Ong *et al.*, "Python Materials Genomics (pymatgen): A robust, open-source python library for materials analysis," *Computational Materials Science*, vol. 68, pp. 314-319, 2013.
- [48] A. Jain *et al.*, "Commentary: The Materials Project: A materials genome approach to accelerating materials innovation," *APL materials*, vol. 1, no. 1, 2013.
- [49] J. P. Perdew, K. Burke, and M. Ernzerhof, "Generalized gradient approximation made simple," *Physical review letters*, vol. 77, no. 18, p. 3865, 1996.
- [50] M. Ångqvist *et al.*, "ICET–a Python library for constructing and sampling alloy cluster expansions," *Advanced Theory and Simulations*, vol. 2, no. 7, p. 1900015, 2019.
- [51] P. M. Larsen, K. W. Jacobsen, and J. Schiøtz, "Rich ground-state chemical ordering in nanoparticles: Exact solution of a model for Ag-Au clusters," *Physical Review Letters*, vol. 120, no. 25, p. 256101, 2018.
- [52] J. Brorsson, A. E. Palmqvist, and P. Erhart, "First-principles study of order—disorder transitions in pseudobinary clathrates," *The Journal of Physical Chemistry C*, vol. 125, no. 41, pp. 22817-22826, 2021.

- [53] A. Benisek and E. Dachs, "The accuracy of standard enthalpies and entropies for phases of petrological interest derived from density-functional calculations," *Contributions to Mineralogy and Petrology*, vol. 173, no. 11, p. 90, 2018.
- [54] A. Togo and I. Tanaka, "First principles phonon calculations in materials science," *Scripta materialia*, vol. 108, pp. 1-5, 2015.
- [55] F. Eriksson, E. Fransson, and P. Erhart, "The Hiphive Package for the extraction of high-order force constants by machine learning," *Advanced Theory and Simulations*, vol. 2, no. 5, p. 1800184, 2019.
- [56] K. Jacob, A. Kumar, G. Rajitha, and Y. Waseda, "Thermodynamic data for Mn3O4, Mn2O3 and MnO2," *High Temperature Materials and Processes*, vol. 30, no. 4, pp. 459-472, 2011.
- [57] K. Jacob, A. Kumar, and Y. Waseda, "Gibbs energy of formation of MnO: measurement and assessment," *Journal of Phase Equilibria and Diffusion*, vol. 29, no. 3, pp. 222-230, 2008.
- [58] C. W. Bale *et al.*, "Reprint of: FactSage thermochemical software and databases, 2010–2016," *Calphad*, vol. 55, pp. 1-19, 2016.
- [59] P. Hofmann, Solid state physics: an introduction. John Wiley & Sons, 2022.
- [60] A. D. Becke and E. R. Johnson, "A simple effective potential for exchange," *The Journal of chemical physics*, vol. 124, no. 22, 2006.
- [61] F. Tran, P. Blaha, and K. Schwarz, "Band gap calculations with Becke–Johnson exchange potential," *Journal of Physics: Condensed Matter*, vol. 19, no. 19, p. 196208, 2007.
- [62] A. M. Ganose, A. J. Jackson, and D. O. Scanlon, "sumo: Command-line tools for plotting and analysis of periodic* ab initio* calculations," *Journal of Open Source Software*, vol. 3, no. 28, p. 717, 2018.
- [63] K. Poeppelmeier, M. Leonowicz, J. Scanlon, J. Longo, and W. Yelon, "Structure determination of CaMnO3 and CaMnO2. 5 by X-ray and neutron methods," *Journal of Solid State Chemistry*, vol. 45, no. 1, pp. 71-79, 1982.
- [64] O. Merkulov *et al.*, "Impact of oxygen vacancies on thermal and electronic transport of donor-doped CaMnO3-δ," *Journal of Solid State Chemistry*, vol. 326, p. 124231, 2023.
- [65] E. I. Goldyreva, I. A. Leonidov, M. V. Patrakeev, and V. L. Kozhevnikov, "Thermodynamics of oxygen in CaMnO3– δ," *Journal of Solid State Electrochemistry*, vol. 17, no. 12, pp. 3185-3190, 2013.
- [66] E. Wollan and W. Koehler, "Neutron diffraction study of the magnetic properties of the series of perovskite-type Compounds [(1– x) La, x Ca] Mn O 3," *Physical Review*, vol. 100, no. 2, p. 545, 1955.
- [67] E. Abdel-Khalek, E. Mohamed, and Y. A. Ismail, "Study the role of oxygen vacancies and Mn oxidation states in nonstoichiometric CaMnO3-δ perovskite nanoparticles," *Journal of Sol-Gel Science and Technology*, pp. 1-12, 2025.
- [68] J. Jung *et al.*, "Determination of electronic band structures of CaMnO 3 and LaMnO 3 using optical-conductivity analyses," *Physical Review B*, vol. 55, no. 23, p. 15489, 1997.
- [69] R. Panigrahi and B. S. Mallik, "Ionic conduction and cathodic properties of CaMO3 (M= Fe and Mn) electrode materials via molecular dynamics and first-principles simulations," *Journal of Physics and Chemistry of Solids*, vol. 196, p. 112384, 2025.
- [70] R. Søndenå, S. Stølen, P. Ravindran, T. Grande, and N. L. Allan, "Corner-versus face-sharing octahedra in A Mn O 3 perovskites (A= Ca, Sr, and Ba)," *Physical Review B—Condensed Matter and Materials Physics*, vol. 75, no. 18, p. 184105, 2007.

- [71] U. Aschauer, R. Pfenninger, S. M. Selbach, T. Grande, and N. A. Spaldin, "Strain-controlled oxygen vacancy formation and ordering in CaMnO 3," *Physical Review B—Condensed Matter and Materials Physics*, vol. 88, no. 5, p. 054111, 2013.
- [72] K. Momma and F. Izumi, "VESTA 3 for three-dimensional visualization of crystal, volumetric and morphology data," *Applied Crystallography*, vol. 44, no. 6, pp. 1272-1276, 2011.
- [73] C. C. Chiang and K. R. Poeppelmeier, "Structural investigation of oxygen-deficient perovskite CaMnO2. 75," *Materials Letters*, vol. 12, no. 1-2, pp. 102-108, 1991.
- [74] N. Chihaoui, R. Dhahri, M. Bejar, E. Dharhi, L. Costa, and M. Graça, "Electrical and dielectric properties of the Ca2MnO4– δ system," *Solid state communications*, vol. 151, no. 19, pp. 1331-1335, 2011.
- [75] M. Leonowicz, K. R. Poeppelmeier, and J. Longo, "Structure determination of Ca2MnO4 and Ca2MnO3. 5 by X-ray and neutron methods," *Journal of Solid State Chemistry*, vol. 59, no. 1, pp. 71-80, 1985.
- [76] Y. Surace, M. Simões, J. Eilertsen, L. Karvonen, S. Pokrant, and A. Weidenkaff, "Functionalization of Ca2MnO4–δ by controlled calcium extraction: Activation for electrochemical Li intercalation," *Solid State Ionics*, vol. 266, pp. 36-43, 2014.
- [77] J. Takahashi and N. Kamegashira, "X-ray structural study of calcium manganese oxide by rietveld analysis at high temperatures [Ca2MnO4. 00]," *Materials research bulletin*, vol. 28, no. 6, pp. 565-573, 1993.
- [78] N. Guiblin, D. Grebille, H. Leligny, and C. Martin, "Ca3Mn2O7," *Crystal Structure Communications*, vol. 58, no. 1, pp. i3-i5, 2002.